Modeling postconvective submesoscale coherent vortices in the northwestern Mediterranean Sea

Pierre Damien, Anthony Bosse, Pierre Testor, Patrick Marsaleix, Claude Estournel

Modeling Postconvective Submesoscale Coherent Vortices in the Northwestern Mediterranean Sea

P. Damien[1,2], A. Bosse[3], P. Testor[3], P. Marsaleix[2], and C. Estournel[2]

[1]Departamento de Oceanografia Fisica, CICESE, Ensenada, Baja California, Mexico, [2]Laboratoire d'Aérologie, Université de Toulouse, CNRS, UPS, France, [3]LOCEAN, UMR 7159, CNRS-IRD-UPMC, MNHN, Paris, France

Abstract For the first time, the formation of submesoscale coherent vortices (SCVs) during intermediate and deep convection events is documented in a realistic high-resolution (1 km) numerical simulation of the oceanic circulation in the northwestern Mediterranean Sea. Winter intermediate and deep convection leads to the formation of anticyclonic and cyclonic eddies with lifetimes exceeding 1 year. By focusing on three typical eddies, the main characteristics of such vortices are discussed. The anticyclonic eddies are typical of SCVs observed in deep convection areas so far. They are characterized by a small radius (∼6.5 km) and orbital peak velocities of about 7 cm/s located at great depth (∼1500 m) or intermediate depth (∼500 m). The cyclonic vortices show very similar characteristics, such as a high Rossby number (∼0.4), but with surface-intensified structures. The long lifetimes of both anticyclonic and cyclonic eddies reflect very slow diffusive processes between their core and their surroundings and a strong resistance to external perturbations. These long-lived eddies are found to participate in the spreading of a significant portion (from 15 to 35%) of the convected waters in the Gulf of Lions and contribute to the ventilation of the deep basin.

1. Introduction

The northwestern Mediterranean Sea (Gulf of Lions area shown on Figure 1) is, along with the Weddell, Labrador, and Greenland Seas, known to be one of the few sites in the world where open ocean deep convection can occur [*Marshall and Schott*, 1999]. In all these places, the phenomenon is similar: during wintertime, cooling and evaporation act on the surface waters over an area preconditioned by a basin-scale cyclonic circulation. This preconditioning is a necessary condition for open ocean deep convection to occur, as isopycnals are thus raised toward the surface, bringing dense waters close to the surface. In the Gulf of Lions, buoyancy losses are mainly the consequences of intense dry and cold winds: Mistral and Tramontane. These winds induce particularly strong buoyancy losses at the surface, which reach up to 800 W/m^2 during storms [*Mertens and Schott*, 1998], thus decreasing the potential temperature of the surface waters and increasing their salinity. The surface density progressively increases and even exceeds the density of the water underneath. In response to this gravitationally unstable situation, vertical convective mixing arises and restores the stability by decreasing the buoyancy of the water column. This progressively leads to deepening of the mixed layer depth (MLD). If buoyancy losses are strong and/or last long enough, the mixed layer can reach great depths, even the sea floor (located at ∼2500 m depth in the Gulf of Lions) [*Houpert et al*., 2016]. A patch composed of weakly stratified waters is progressively created. This mixed patch of newly formed waters is maintained during wintertime by the strong buoyancy losses at the air-sea interface. When the intensity of the buoyancy losses decreases, baroclinic instabilities start to develop and tend to break up the mixed patch through lateral buoyancy exchanges [*Gascard*, 1978; *Gascard and Clarke*, 1983]. The newly formed waters are thus dispersed in the surrounding stratified environment, during the so-called spreading/restratification phase of the deep convection phenomenon [*MEDOC-Group*, 1970].

In the northwestern Mediterranean Sea, open ocean convection leads to the formation of two main water types, Winter Intermediate Waters (WIW) and Western Mediterranean Deep Waters (WMDW), depending on the depth reached by the mixed layer. Their generation can be described by successive steps. Under the cooling imposed by the air-sea fluxes in winter, the characteristics of the Modified Atlantic Waters (MAW) [*Millot*, 1999] lying in the upper ocean are modified. In a first step, the newly formed waters are

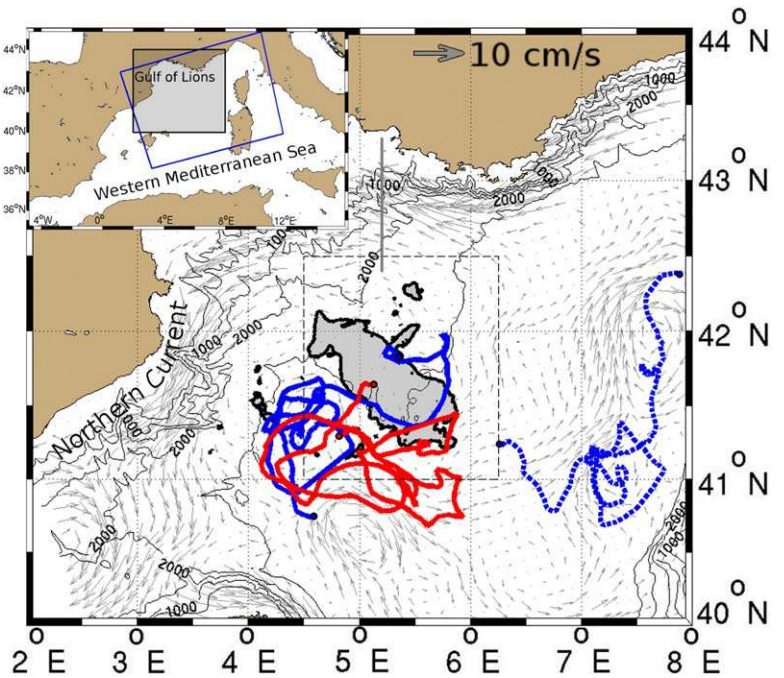

Figure 1. Bathymetric map of the Gulf of Lions. The deep convection area (MLD > 1000 m) in winter 2009 is indicated by the gray patch. The trajectories of three postconvective eddies are represented: an anticyclone (A^{DW}, blue line) and a cyclone (C^{DW}, red line) of deep waters, and an anticyclone (A^{WiW}, dashed blue line) of WIW. The modeled annual average velocity field at 100 m depth is also represented by grey arrows. The dotted box sets the geographical limits of the map presented in Figure 2. The gray line along meridian 5°30′E sets the location of the transect presented in Figure 6. The insert delineates the modeling domain (blue box) and the location of the map (gray box).

characterized by a potential temperature minimum ($11.5°C < \theta < 12.9°C$) and low salinity ($37.7 < S < 38.4$) between 0 and 200 m and are called WIW [*Salat and Font*, 1987; *Pinot and Ganachaud*, 1999; *Vargas-Yanez et al*., 2012]. WIW, which are denser than MAW, can eventually become isolated from interactions with the atmosphere forming a modal water mass that spreads in the basin at its equilibrium depth. If the MLD goes deeper than 400 m, it incorporates the warm, salty Levantine Intermediate Waters (LIW), which can be found in the northwestern Mediterranean Sea between 400 and 800 m [*Millot*, 1999]. By vertical entrainment, the temperature of the MLD no longer decreases but increases, as does the salinity. Below this layer, the ocean stratification is weaker and the MLD can quickly reach great depth and mix the prevailing Western Mediterranean Deep Waters (WMDW). This results in the formation of new Western Mediterranean Deep Waters (nWMDW) [*Testor and Gascard*, 2003]. Their temperature/salinity properties depend on the depth reached by the mixed layer but are usually close to those of old WMDW ($12.75°C < \theta < 12.91°C$ and $38.44 < S < 38.49$) [*Millot*, 1999; *Rixen et al*., 2005; *Schroeder et al*., 2006; *Houpert et al*., 2016]. Figure 2 gives in a schematic view the water masses described with their T-S characteristics.

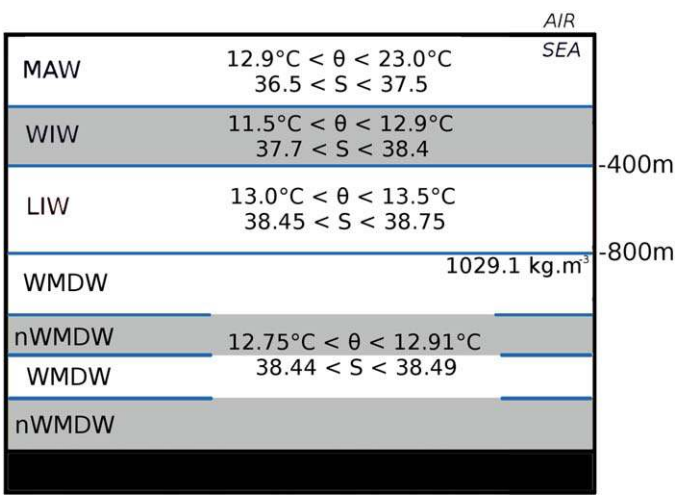

Figure 2. Schematic representation of water masses in the northwestern Mediterranean Sea with their characteristics [*Millot*, 1999; *Schroeder et al*., 2006; *Houpert et al*., 2016]. Waters formed by winter convective events are represented with gray shading.

As the newly formed waters spread out of the convection zone, a

significant proportion can be trapped within submesoscale eddies. Such eddies have been observed in the Greenland Sea [*Gascard et al*., 2002; *Budéus et al*., 2004], the Labrador Sea [*Pickart et al*., 1996; *Lilly et al*., 2003], and the Mediterranean Sea [*Testor and Gascard*, 2003, 2006] with similar dynamical characteristics. These so-called submesoscale coherent vortices (SCVs) [*McWilliams*, 1985] are mostly anticyclonic with a singular vertical structure: relatively homogeneous temperature-salinity and a weakly stratified core associated with a lens-shaped deformation of the isopycnals. Their horizontal size is often smaller than the first baroclinic deformation radius. They are qualified as coherent as they have been observed to survive for more than 1 year [*Armi et al*., 1988; *Testor and Gascard*, 2003; *Ronski and Budéus*, 2006]. In the northwestern Mediterranean Sea, recent in situ observations in the basin [*Testor et al*., 2017] allowed a much better dynamical characterization of such small-scale structures [*Testor and Gascard*, 2003, 2006; *Bosse et al*., 2015, 2016].

To understand the formation and propagation of postconvective eddies, numerical simulations have already been carried out in very idealized [*Jones and Marshall*, 1993; *Akitomo*, 2010] or more realistic but still simplified configurations [*Oliver et al*., 2008]. Based on a numerical simulation at very high resolution of two convective winters in the northwestern Mediterranean Sea using realistic bathymetry, initial oceanic conditions and air/sea fluxes, the present paper examines the spreading, by submesoscale vortices, of the water masses (WIW and nWMDW) formed by the winter vertical mixing. We give the first demonstration that such eddies, which have always been considered as subgrid phenomena until today, can be explicitly resolved thanks to advances in modeling. The objectives of this study are first to show that a regional high-resolution model is a relevant tool to describe submesoscale vortices under fully realistic conditions, then to take advantage of the comprehensive 4-D vision provided by the model to fill the gaps of in situ observations in terms of continuous tracking of the structures throughout their life, and finally, to assess their integral contribution to the spreading of newly formed water. We first describe such eddies from their generation at the edge of the convective patch to their dissipation, and then consider their large scale implication in the functioning of the northwestern Mediterranean Sea.

2. Method

We use the 3-D ocean circulation model SYMPHONIE [*Marsaleix et al*., 2008, 2009, 2011, 2012] based on the Navier-Stokes primitive equations solved on an Arakawa curvilinear C-grid under the hydrostatic and Boussinesq approximations. The model makes use of an energy conserving finite difference method described by *Marsaleix et al*. [2008], a Leap-Frog time stepping scheme combined with a Laplacian filter [*Marsaleix et al*., 2012], a Jacobian pressure gradient scheme [*Marsaleix et al*., 2009], the equation of state of *Jackett et al*. [2006] with the implementation described in *Marsaleix et al*. [2011], and the K-epsilon turbulence scheme with the implementation described in *Michaud et al*. [2012] and *Estournel and Guedalia* [1987]. Horizontal advection and diffusion of tracers are computed using the Leap-Frog version of the UP3 scheme described in *Marchesiello et al*. [2009]. In areas of low turbulence, vertical diffusivity is possibly controlled more by the diffusion induced by the hyperdiffusivity term of the UP3 advection scheme rather than by the closure turbulent scheme. Indeed, *Marchesiello et al*. [2009] estimate that the UP3-induced diapycnal diffusivity could be of the order of 0.01 m^2/s for resolution finer than 1 km. An equivalent horizontal Laplacian diffusivity of about 0.02 m^2/s is estimated in our case. Horizontal advection and diffusion of momentum are each computed with a fourth order centered biharmonic scheme. The biharmonic viscosity of momentum is not constant. Small scales are indeed preferentially targeted by a Smagorinsky-like formulation derived from *Griffies and Hallberg* [2000]. An equivalent Laplacian viscosity [*Lee et al*., 2002] of about 0.01 m^2/s is estimated in our case. According to *Griffies and Hallberg* [2000], this approach leads to a better representation of small-scale processes and, in the present work, appeared decisive in the successful long-term simulations of SCVs. The boundary conditions, based on radiation conditions combined with nudging conditions, are described in *Marsaleix et al*. [2006]. The nudging zone is 20 grid node wide. Related restoring time scales are 0.1 and 1 day respectively for barotropic and baroclinic currents. Several other applications of this model in the northwestern Mediterranean Sea can be found in *Estournel et al*. [2009, 2016], *Petrenko et al*. [2008], and *Rubio et al*. [2009]. The model domain extends from the Balearic Sea to the Tyrrhenian Sea and thus encompasses a significantly larger region than only the deep convection zone (Figure 1). The grid has 40 generalized σ-levels on the vertical. Sigma levels are regularly spaced on the continental shelf (and more generally wherever the sea bottom is above -100 m). Irregularly spaced levels are used everywhere else in

order to maintain a suitable resolution within the first hundred meters below the surface. In the deep convection zone, above the abyssal plain (which has a depth of about 2500 m), the vertical resolution is 2.5 m near the surface and increases to 150 m at about −1700 m depth. In order to achieve good resolution of the processes leading to the formation of the vortices from a homogeneous water column, three quarters of the layers are concentrated in the first 1000 m. The horizontal resolution is 1 km in order to represent mesoscale and submesoscale eddies, the internal deformation radius being ∼10 km in this area due to the low stratification [*Testor and Gascard*, 2006]. Since the convective plumes involved in the winter convection events are nonhydrostatic and of very small scale (∼1 km) [see *Marshall and Schott*, 1999], they cannot be resolved by such a model and their effects must be parameterized. In case of buoyancy losses at the air-sea interface, a nonpenetrative adjustment algorithm distributes those losses throughout the MLD. The parametrized mixing process is then instantaneous and adiabatic. Radiative, momentum, heat and salt fluxes at the air-sea interface are provided by the ALADIN-Climat atmospheric reanalysis at 12 km horizontal resolution [*Herrmann et al*., 2011]. Initial conditions and open boundary conditions are given by a global simulation of the Mediterranean Sea at 1/12° (∼7 km) resolution, forced by the same atmospheric reanalysis [*Beuvier et al*., 2012]. Daily measured runoffs of the five major rivers of the Gulf of Lions are prescribed on the basis of observations (http://www.hydro.eaufrance.fr) over the simulated period. The simulation starts in January 2008 and lasts 3 years, so two winter convective events are simulated. The model can thus spin up for approximately 1 year and overtake transient processes before the first convective event occurs.

The eddy detection and tracking algorithm developed by *Nencioli et al*. [2010] is applied to daily-averaged model outputs. It is based on the particular horizontal velocity fields associated with such vortices and has been successfully applied to several high-resolution products [*Dong et al*., 2012; *Barbosa Aguiar et al*., 2013]. The eddies we intend to track can be strongly baroclinic and so might be not detectable over the whole water column. Therefore, all variables (temperature, salinity, and velocities) are linearly interpolated on two specific isopycnal levels ($\sigma 0 = 29.0$ kg m^{-3} to detect vortices with a WIW core and $\sigma 1 = 29.1$ kg m^{-3} to detect vortices with a dense water core, where σ stands for potential density anomaly with respect to the surface). The algorithm is then applied to the resulting 2-D fields. Moreover, as the position of each vortex center is known, north-south and west-east sections are produced every day to show the 4-D evolution of each vortex.

3. Formation of Eddies at the Rim of the Convection Zone

The simulation of the convection event of winter 2008/2009 is consistent with the chronology described in the introduction. From October 2008, the water column stability gradually weakens under the strong buoyancy loss due to intense atmospheric cooling and evaporation. The mixed layer progressively deepens until the LIW layer, characterized by a temperature and salinity maximum between −400 and −800 m, is destroyed on 11 February 2009 (Figures 3.1 and 4.1). At this date, the LIW have almost vanished in the deep convection area, as shown by the vertical structure of the convection area (Figures 4.1a and 4.1b between 25 and 60 km) and the density anomaly of the mixed layer is still slightly lower than the threshold of 29.1 kg m^{-3}. This happens after approximately 4 months of negative heat budget at the air-sea interface.

During the following phase of deep mixing, the area where the mixed layer is deeper than 2000 m reaches a large value (>1800 km^2). In Figure 3.2, corresponding to 16 February, this area is marked with a black line contour (Figure 3.2b). Observations confirm that convection reached ∼2300 m depth during wintertime in 2009 and 2010 [*Houpert et al*., 2016]. A very sharp density front separates the mixed patch from the surrounding stratified waters. The vertical structure revealed by transects (Figure 4.3) presents isopycnals that are almost vertical at the rim of the convection area (see isopycnal 29.1 kg m^{-3} at 35 and 45 km). They are maintained in this state by the strong buoyancy loss at the air-sea interface. When the atmospheric forcing decreases in intensity, the front becomes baroclinically unstable and the mixed patch starts to break up. On 16 February (Figure 3.2a), the front is already meandering with a ∼10 km wavelength characterized by alternating positive and negative relative vorticity ($|\zeta| = |dv/dx - du/dy| > 0.4f$, where f is the planetary vorticity, (u,v) the eastward and northward components of the current, and (x,y) the geographical coordinates). The perturbation then grows through the conversion of potential energy into eddy kinetic energy. At a final stage, shown in Figures 3.3 and 3.4, cyclonic and anticyclonic vortices are generated (highlighted by red and blue circles on Figures 3.3b and 3.4b).

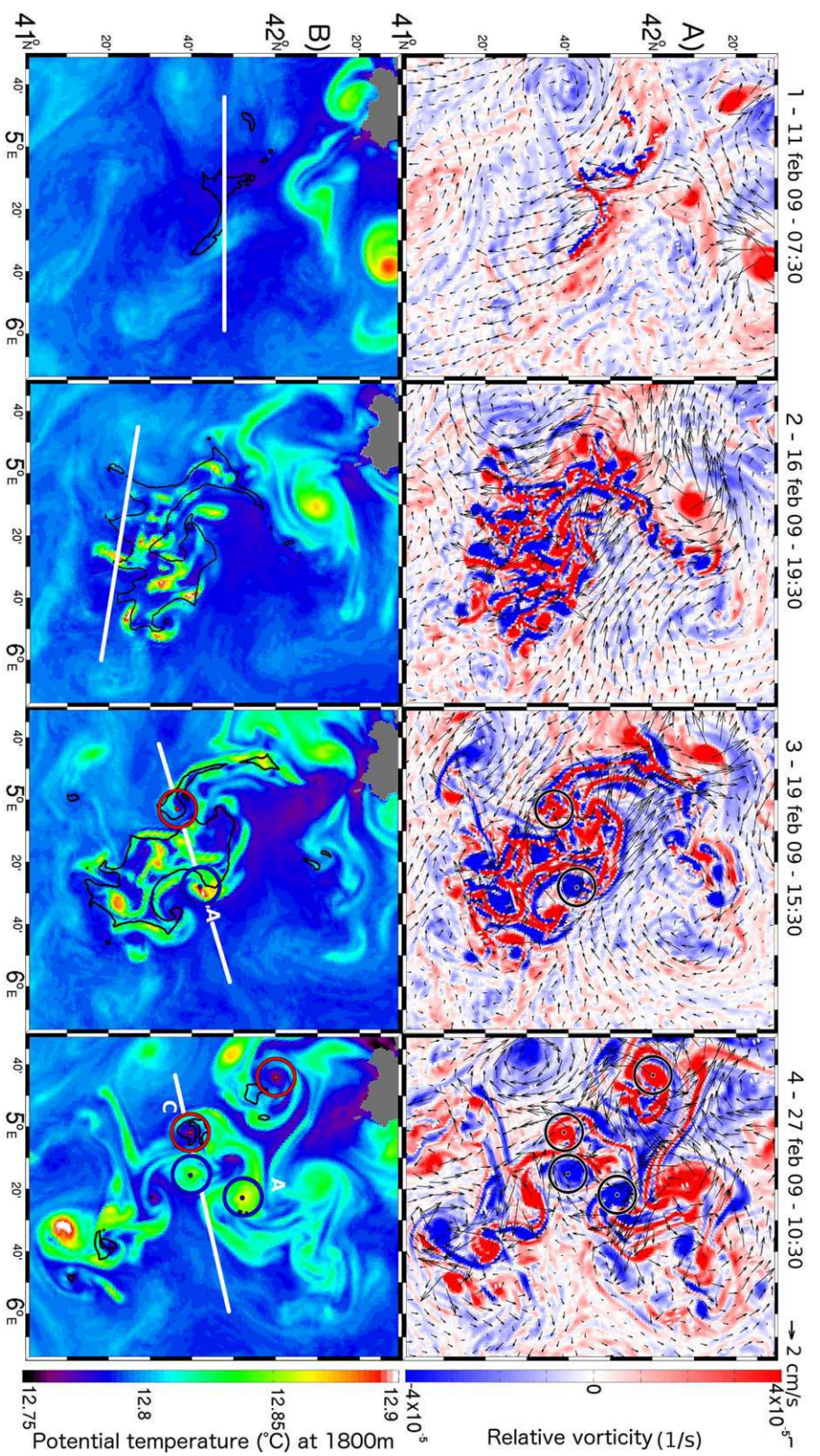

Figure 3. Temporal evolution at important stages of the eddy formation. (a) Relative vorticity on density anomaly $\sigma 1 = 29.1$ kg m^{-3} and velocity field (black arrows) and (b) potential temperature at 1800 m depth and 2000 m mixed layer depth contour (black line). The circles represent the cyclone labeled C^{DW} (in red) and the anticyclone labeled A^{DW} (in blue). The gray shaded area shows where the seabed is above 1800 m. The white lines (Figure 3b) highlight the location of the vertical transects shown in Figure 4.

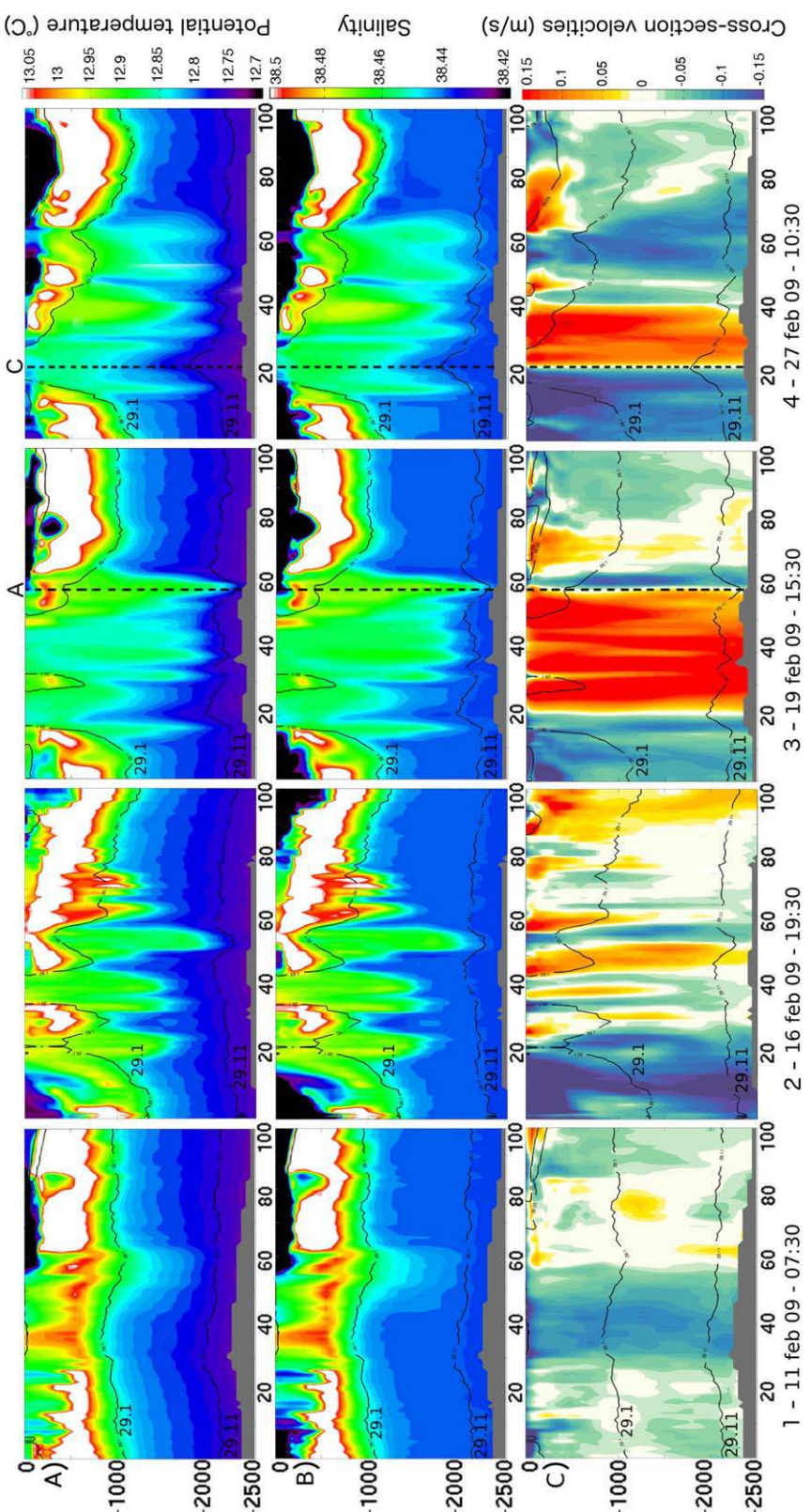

Figure 4. Temporal evolution at important stages of vertical section along the white lines shown in Figure 3: (a) potential temperature, (b) salinity, and (c) cross-section velocity transects. The full black lines indicate the density anomaly contours and the vertical dashed lines the position of C^{DW} and A^{DW}.

Anticyclonic eddies are characterized by a negative relative vorticity (Figure 3a). At 1800 m depth, the potential temperature of their core ranges between 12.85 and 12.90°C (Figure 3b), close to the potential temperature of the WMDW that surround them but slightly warmer. It corresponds to the potential temperature of nWMDW resulting from vertical mixing involving the MAW, the LIW, and part of the WMDW. The warm anomaly characterizing the anticyclonic eddies has been observed in many field experiments carried out in this area [*Testor and Gascard*, 2003; *Bosse et al*. 2016; *Schroeder et al*., 2008; *Testor et al*., 2017]. When baroclinic instability waves grow up at the edge of the deep convection zone, parts of the mixed patch are injected into the stratified surroundings and find their equilibrium near their level of neutral buoyancy. The dynamical adjustment generates an anticyclonic circulation that further preserves the weak stratification of the fluid parcel and its low potential vorticity (PV), as described by *McWilliams* [1988]. As the fluid parcel crosses the front, it becomes progressively isolated from the atmosphere and, in the absence of forcing and dissipation, the Ertel's potential vorticity, defined as $\frac{1}{\rho}\overrightarrow{grad}(\rho)\cdot(f\vec{k}+\vec{\zeta})$, is a Lagrangian conservative variable [*Ertel and Rossby*, 1949], where ρ is the potential density, f the Coriolis parameter, and ζ the relative vorticity. Transects crossing the eddies are indicated by white lines in Figure 3b, reveal their vertical structure (Figure 4) in the model. The anticyclonic eddies exhibit depth-intensified velocities visible in Figure 4.3c at $\sim$60 km and Figure 4.4c at $\sim$40 km. Note that similar warm cores can be seen on Figure 3b to the north but, unlike to the ones discussed above, they result from the instability of the Northern Current, which is the branch of the general cyclonic circulation flowing along the Gulf of Lions (Figure 1). They have a cyclonic signature (Figure 3a) and are not the subject of this study.

Cyclonic eddies characterized by a positive relative vorticity can be seen in Figure 3. At 1800 m depth, the potential temperature of their core is lower than 12.78°C, slightly colder than the surrounding waters (Figure 3b). The vertical structure of these cyclones exhibits a noteworthy doming of isopycnals (Figure 4 at $\sim$20 km in parts 3a and 4a). Isopycnal 29.10 kg m^{-3} reaches the surface and isopycnal 29.11 kg m^{-3} shows a $\sim$200 m upward displacement.

The formation of the anticyclonic and cyclonic eddies seems closely linked as they self-organize in pairs as shown in Figures 3.3 and 3.4. The cyclonic component of each pair is indicated by a red circle (Figure 3b) and the anticyclonic component by a blue circle. The location of the transects is chosen in order to cross the dipoles during their formation and the vertical section is revealed in Figures 4.3 and 4.4. The two structures are generated together, side-by-side, and then separate. This formation in pairs is very similar to the formation of hetons. According to the heton formation theory developed by *Legg and Marshall* [1993] and *Legg et al*. [1996], as a mixed parcel is subducted, it gains an anticyclonic rotation at depth while a cyclonic rotation develops above by conservation of potential vorticity. Then, the anticyclone and the cyclone separate and form a dipole. The anticyclone is a weakly stratified subsurface eddy similar to an anticyclonic SCV and the cyclone has a dynamical structure that is intensified at the surface. This duality is shown on the transects of Figure 4.4: the cyclone (at $\sim$20 km and highlighted by the vertical dashed line) is characterized by a velocity that is intensified at the surface while the anticyclone (at $\sim$40 km) has a lenticular shape with a velocity maximum between 300 and 1000 m depth. In their simulation, *Legg et al*. [1996] described the formation of such hetons and our simulation is in good agreement with their results. In a fully realistic case, once the subsurface anticyclonic eddies form, they become isolated from the atmospheric forcing by a surface stratified layer. In contrast, the surface-intensified cyclones remain sensitive to surface buoyancy losses. Globally, this scenario is consistent with the idealized simulations of baroclinic instability development leading to the formation of eddies performed by *Marshall and Schott* [1999] and *Akitomo* [2010], and with laboratory experiments by *Narimousa* [1998].

The WIW is clearly observable in Figure 4 between 0 and 300 m depth. Its low temperature (below 12.90°C) and low salinity (below 38.40) make it easily recognizable (see, for example, the top right parts of Figures 4.4a and 4.4b on 27 February). This water mass is formed under shallow convection conditions either at the beginning of the convective event or around the deep convection zone (Figure 5). The mixed layer often reaches great depths in the center of the basin, where local preconditioning is the most intense. Elsewhere, the preconditioning effects being less intense, convection tends to be restricted to the formation of WIW. Generation of anticyclonic eddies with WIW cores is also observed in the model. Their formation follows a process similar to that of nWMDW anticyclonic eddies. A parcel of WIW is subducted into a more stratified region and acquires an anticyclonic vorticity by dynamical adjustment (Figure 6). Beside these processes linked to open sea convection, it can be noticed that a significant amount of cold, dense waters is formed

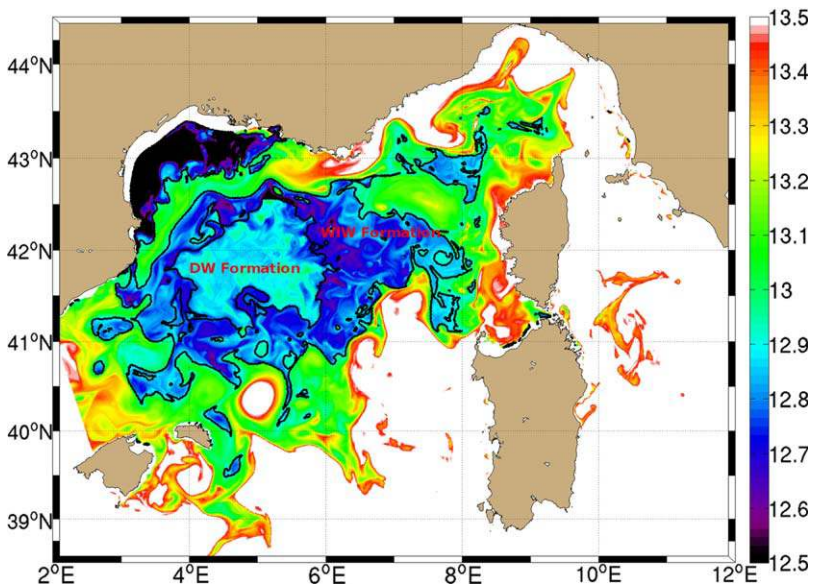

Figure 5. Winter potential temperature at 50 m depth in early February 2009. The area of deep water formation offshore is surrounded by a zone of WIW formation characterized by a colder signature.

on the shallow continental shelf of the Gulf of Lions (Figure 5). During particular winters, like 2012, these waters can then cascade down to the abyssal plain and spread out toward the ocean basin [*Durrieu de Madron et al*., 2013]. This process contributing to the renewal of deep waters and to shelf/deep ocean exchanges [*Durrieu de Madron et al*., 2013; *Ulses et al*., 2008] is not part of the present study.

To summarize, the convective events simulated in the Gulf of Lions lead to the formation of numerous eddies. We will further classify them into three categories: anticyclonic eddies of nWMDW or of WIW, and cyclonic eddies. This classification also agrees with in situ observations [*Bosse et al*., 2016]. Once the restratification phase begins, these eddies can transport the water masses trapped in their core over long distances. Dynamical barriers isolate them from the surrounding waters, notably from the stratified surface layers.

4. Characteristics of the SCVs

In order to study the characteristics of postconvective eddies, we will focus on three individual vortices: an anticyclone (A^{DW}) carrying nWMDW, an anticyclone of WIW (A^{WIW}), and a cyclone (C^{DW}). These vortices are representative of the three categories of long-lived eddies formed after the convective events in the simulation. Their trajectories are drawn in Figure 1 and the early life stages of A^{DW} and C^{DW} are described in Figure 3.

4.1. Mean Hydrographical and Dynamical Characteristics

A vortex lifetime is defined as the difference between the date at which the vortex is detected for the last time (eddy destruction) and the date at which the vortex is detected for the first time (eddy generation). To describe the mean properties of the eddies, west-east and south-north transects crossing the core of each structure are recorded at each model output and averaged over its lifetime. This method provides a composite image of each eddy and allows a global overview of their mean hydrographical and dynamical characteristics. For each vortex, Figure 7 provides the composite vertical section of average potential temperature (a), salinity (b), the mean orbital velocity V (c), and PV (d). The radius, R, of each vortex is defined as the distance from its center (defined as the zero velocity position) to the peak velocity V_{max}. Its thickness, H, is defined as the height over which orbital velocities are larger than 65% of its maximum value. The Rossby number is then computed as: $R_o = \zeta/f$, where f is the local Coriolis parameter.

The anticyclone A^{DW} has a mean radius, R, of 6.5 km, a thickness, H, of 2150 m and its core is located at 1450 m depth. The core center is defined by the depth at which isopycnals are flat while a downward (resp. upward) displacement of isopycnals occurs below (resp. above) the core depth. The core is weakly stratified

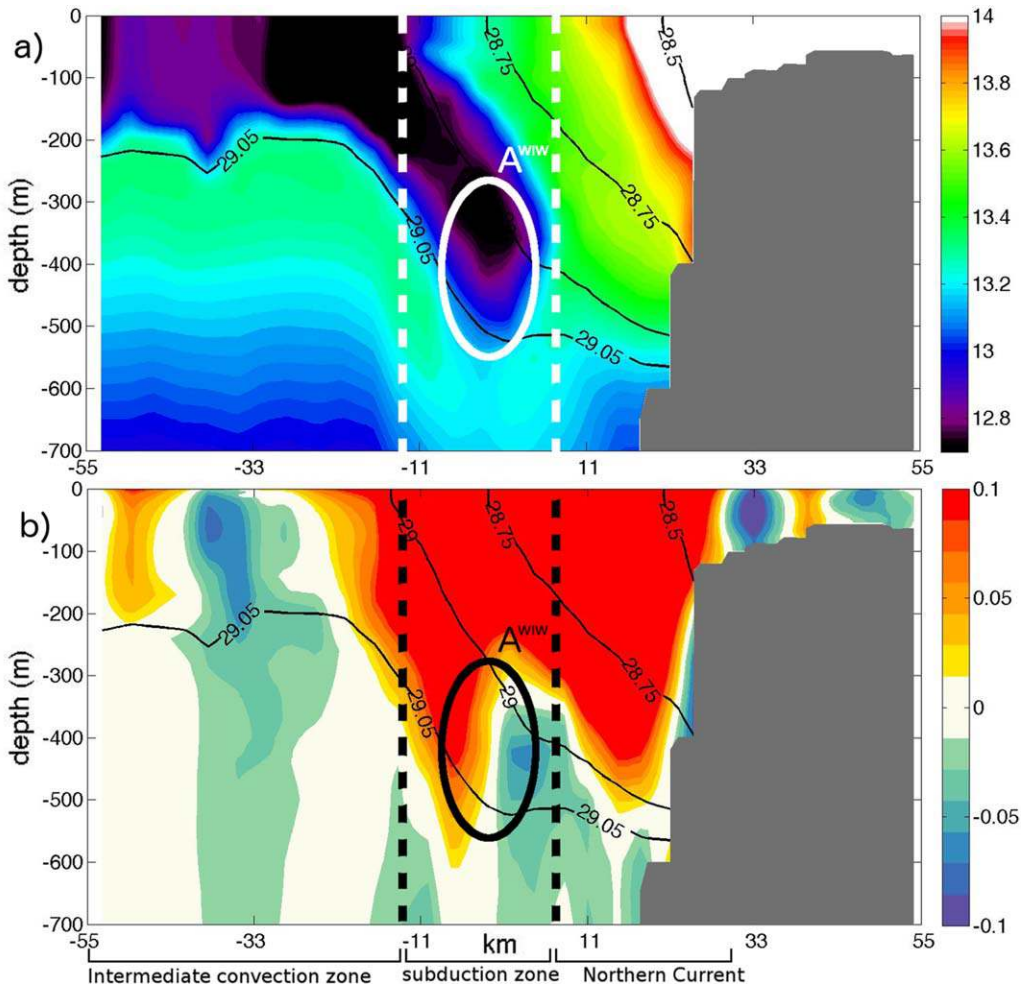

Figure 6. Formation of an anticyclonic WIW SCV by subduction of a cold water parcel across a front located north of the convection zone (shown in Figure 1). (top) Potential temperature and (bottom) orthogonal velocity sections are shown with potential density anomaly contours (black lines). The vertical dashed lines indicate the position of the SCV core.

with nearly homogeneous characteristics of potential temperature (∼12.88°C, Figure 7.1a) and salinity (∼38.46, Figure 7.1b). This is warmer (∼+0.05°C) and saltier (∼+0.012) than its surroundings at the core depth. This positive heat/salt anomaly is even more marked at large depths (up to ∼+0.08°C and ∼+0.016). The formation of a warm anomaly at 1800 m associated with negative relative vorticity is clearly visible in Figures 3.3 and 3.4. In terms of T/S characteristics, these deep waters are close to the average values of WMDW, but still slightly warmer and saltier.

The anticyclone A^{DW} exhibits a remarkable density structure typical of anticyclonic submesoscale coherent vortices described by *McWilliams* [1985]. The peak velocity V_{max} of 6.9 cm/s is located at ∼1500 m depth (Figure 7.1c). This corresponds to a Rossby number of −0.23 assuming a rigid-body-like vortex ($\zeta = 2V_{max}/R$). If ζ is computed at the center of the vortex, R_o is even higher, reaching −0.46. Such a high Rossby number, relatively close to unity, means that the eddy is not completely in geostrophic balance. The centrifugal force plays a significant role in the eddy force balance by decreasing the Coriolis force by nearly 10% to balance the pressure force and by accelerating the eddy's anticyclonic rotation. Moreover, the eddy is also recognizable by its local minimum of PV (Figure 7.1d). Its core waters should therefore originate from the convection area where PV is destroyed in winter by the atmospheric forcing and intense vertical mixing. Once restratification occurs, this quantity is then conserved at the first order within the eddy core. The dynamical characteristics of this eddy are very realistic compared to postconvective SCVs described in the Mediterranean Sea using isobaric Lagrangian floats [*Testor and Gascard*, 2006] and more recently using gliders [*Bosse et al*., 2016].

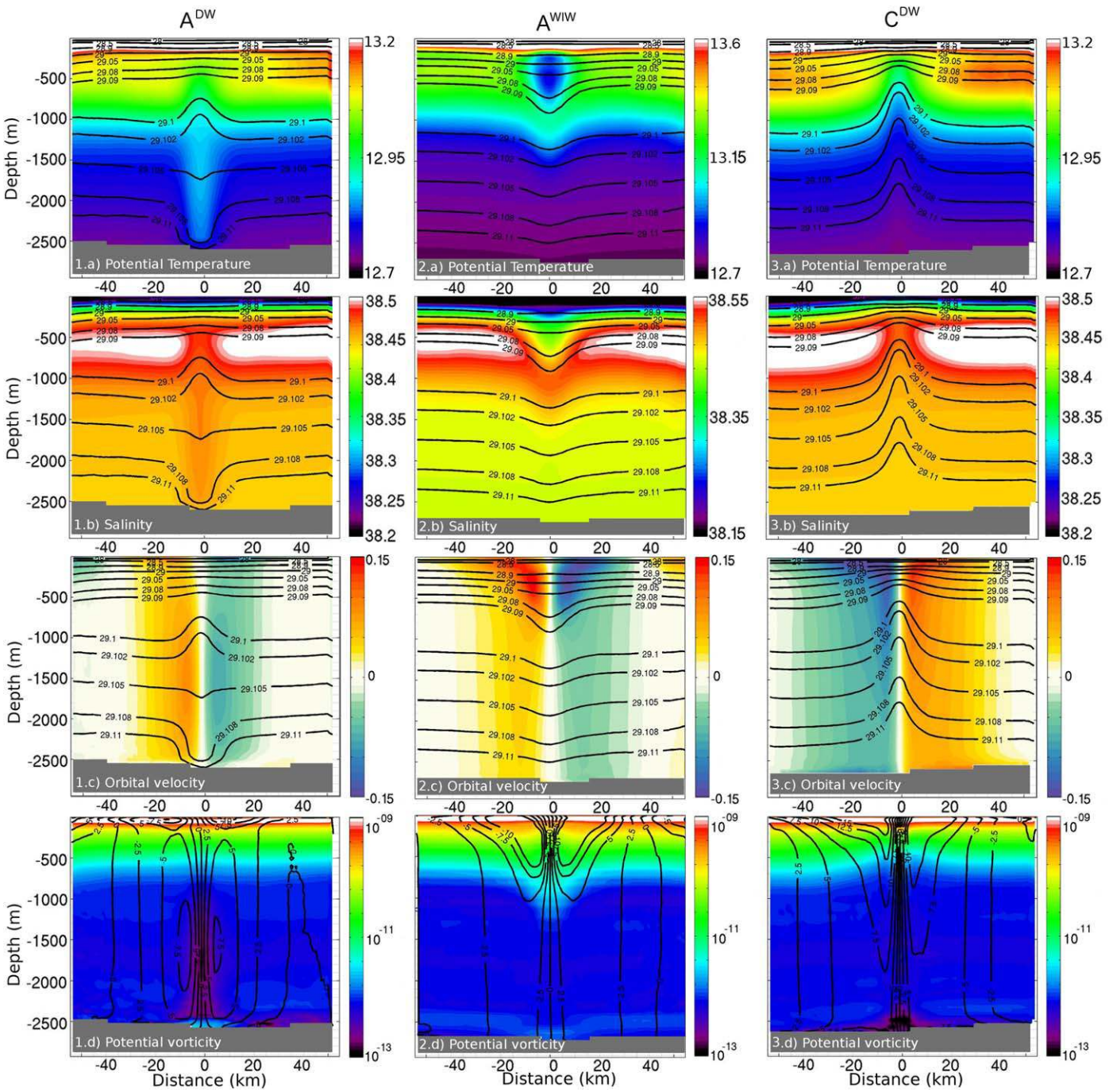

Figure 7. Composite transects of (left column) anticyclone A^{DW}, (middle column) anticyclone A^{WIW}, and (right column) cyclone C^{DW}: (a) potential temperature, (b) salinity, (c) orbital velocities with potential density anomaly contours, and (d) the potential vorticity with orbital velocity contours. The composite images were obtained by averaging west-east and south-north transects crossing the core of each structure at each model output. Color scales are chosen to highlight the hydrographical core of each eddy. The gray shaded area represents the seabed.

The anticyclonic A^{WIW} structure averaged over its lifetime presents a low stratified core at 300 m depth (Figure 7.2). Its mean radius is about 7.5 km and its thickness about 650 m. Its core contains homogeneous waters characterized by a potential temperature of ∼12.87°C (Figure 7.2a) and a salinity of ∼38.4 (Figure 7.2b) typical of WIW formed by shallow winter convection [*Millot*, 1999]. It is thus colder (∼–0.3°C) and fresher (∼–0.12) than its surroundings at its core depth. The eddy core is located just above the layer of LIW, which nearly vanishes at the core position. The pathway and spreading mechanisms of WIW in the

western Mediterranean Sea are still not well understood. In particular, eddies of WIW (call Weddies) have already been observed in the Ligurian Sea [*Gasparini et al*., 1999], the Balearic Sea [*Pinot and Ganachaud*, 1999], and even the Alboran Sea [*Allen et al*., 2008], demonstrating how widespread and coherent these eddies may be.

The peak orbital velocity of anticyclone A^{WIW} is about 12.2 cm/s (Figure 7.2c) which implies a Rossby number of -0.36 (with $\zeta = 2V_{max}/R$). It is clearly an SCV as described by *McWilliams* [1985]. This SCV is highly nonlinear and, in this case, the centrifugal force compensates about 25% of the Coriolis force in the cyclogeostrophic equilibrium. Dynamically, anticyclone A^{WIW} is very similar to A^{DW}, presenting a maximum velocity located at its core depth and an intense negative vorticity.

The average section of cyclonic eddy C^{DW} shows a deep hydrographical core extending from $\sim$400 m depth down to the bottom of the ocean (Figure 7.3, right column). The eddy has a mean radius of 6.1 km, slightly smaller than the internal deformation radius (about 10 km in the area). Its hydrographical core, located near the seabed, is weakly stratified, indicating the presence of a nearly homogeneous water mass. It has a potential temperature of 12.80°C (Figure 7.3a) and a salinity of 38.45 (Figure 7.3b). Since the mixed layer does not reach the bottom of the ocean during its formation (Figure 4.4), no formation of waters occurs in the core of C^{DW}, which is then composed of WMDW. At 2000 m, the waters are colder ($\sim$–0.015°C) and fresher ($\sim$–0.001) than their surroundings. This cold anomaly is explained by the remarkably pronounced doming of deep isopycnals that characterize the cyclone C^{DW} (uplift of $\sim$800 m in deep layers, see Figure 7.3a). Note that the warm, salty LIW almost completely vanishes within the eddy core between 400 and 800 m (Figure 7.3b).

Compared to A^{DW}, the cyclonic eddy presents an intensification of its orbital velocity at the surface, associated with a significant Sea Surface Height (SSH) signature (negative anomaly of the SSH of $\sim$–5 cm on average). A stronger stratification associated with peak orbital currents is located at around 150 m depth well above the low stratified hydrographical core. At that depth, the mean orbital velocity of the eddy is 15.0 cm/s (Figure 7.3c), corresponding to a high relative vorticity and a high Rossby number of $\sim$0.50 (with $\zeta = 2V_{max}/R$). As for anticyclone A^{DW}, the structure is dynamically in cyclogeostrophic equilibrium, the centrifugal force increasing the Coriolis force by about 10%. The sum of these two forces counterbalances the pressure gradient force and leads to smaller rotational velocities compared to the geostrophic balance. Moreover, its radius is of the order of the internal deformation radius or slightly smaller, unlike classical surface mesoscale eddies. Using numerical simulations, *Beuvier et al*. [2012] and *Herrmann et al*. [2008] have highlighted the formation of cyclonic vortices at the rim of the convection zone in the northwestern Mediterranean Sea but with radii ranging from 15 to 40 km. In their simulations, the winter vertical mixing reaches the bottom of the ocean and the cyclones that develop present a core of nWMDW. Their structures look like cones of convected waters as described by *Jones and Marshall* [1993] and *Send and Marshall* [1995]. The hydrographical and dynamical characteristics of C^{DW} are different in our study, as its core contains WMDW and its size is typical of the submesoscale. *Testor and Gascard* [2006] have revealed the presence of small-scale cyclonic eddies with a core of typical WMDW in the northwestern Mediterranean Sea, which are similar to C^{DW}. Numerically resolving such small-scale structures is a challenge requiring horizontal resolution close to 1 km.

4.2. Transport Properties and Diffusion of SCVs

A crucial aspect of SCVs is their long lifetime associated with the very low diffusive processes of their core [*Budéus et al*., 2004]. As they are defined by temperature and salinity anomalies of their core, we can examine how these particular properties evolve with time. The temporal evolution of potential temperature, salinity and orbital velocity at their hydrographical core depth is shown on Figures 8a–8c, 10a–10c, and 12a–12c. We define the potential temperature (respectively salinity) anomaly as the difference between the potential temperature (resp. salinity) inside and outside the core of the eddy (Figures 9a, 11a, and 14a), the area outside the core being defined as the mean state at a distance of 4 to 5 radii from the core.

Figure 1 presents the trajectory of the anticyclone A^{DW} during its lifetime of 339 days while it is advected at a mean velocity of $\sim$3.0 cm/s and stays at less than 140 km from its generation site (Movie S1 in the supporting information). A mesoscale barotropic anticyclonic eddy located east of the Balearic Islands prevents it from drifting southward. This large eddy does not move significantly and has a clear signature on the annual mean velocity at 100 m depth (Figure 1). The lifetime of about 1 year of the simulated SCV A^{DW} is

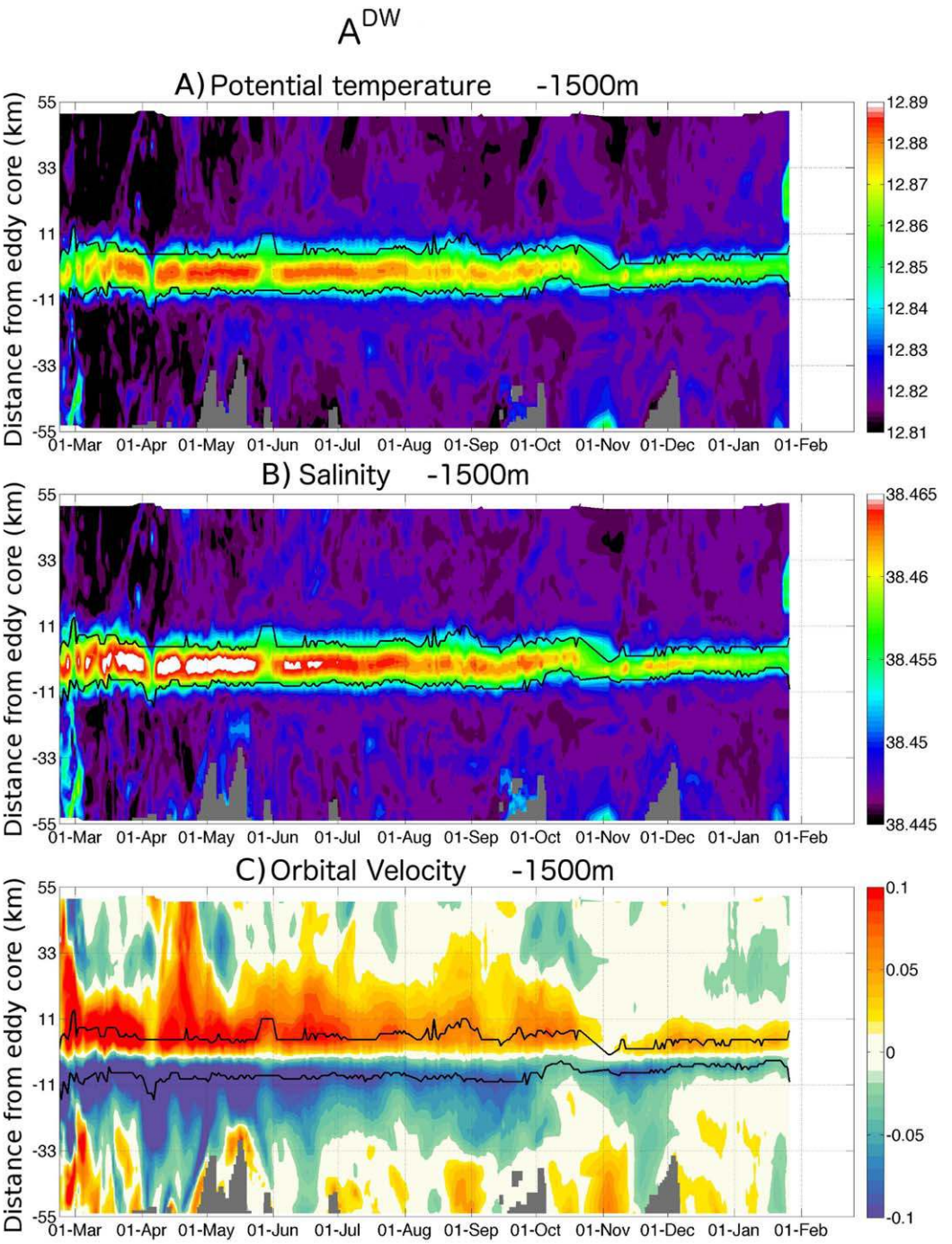

Figure 8. Hovmöller diagrams of (a) potential temperature, (b) salinity, and (c) orbital velocity crossing the core of the anticyclone A^{DW} at 1500 m depth. The black lines show the location of the maximum and minimum of the orbital velocities, which define the eddy diameter at these depths. The gray shaded area shows the position of the seabed.

consistent with the findings of *Testor and Gascard* [2003, 2006]. They were able to observe and follow such eddies in the western Mediterranean Sea for more than 5 months or even a year and a half using isobaric and quasi Lagrangian floats (RAFOS).

Figure 8 shows the evolution of the core properties of anticyclone A^{DW} at 1500 m depth. During the first month of its existence, a brief increase in the eddy potential temperature and salinity characteristics is

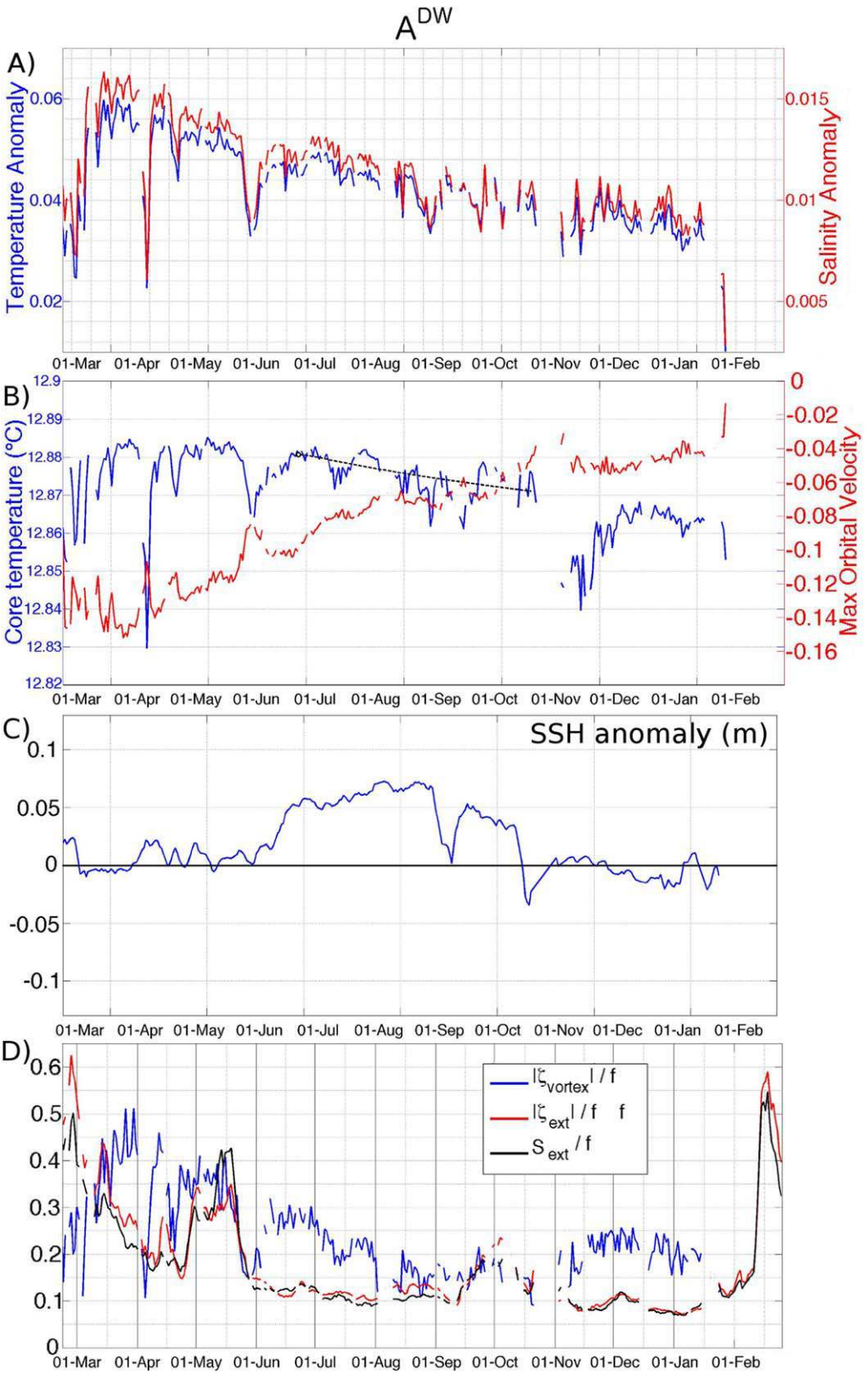

Figure 9. (a) Temporal evolution of temperature (in blue) and salinity (in red) anomalies associated with A^{DW} at 1500 m depth. (b) Temporal evolution of the temperature in the center of the vortex (in blue) and the maximum orbital velocity observed along the SCV transects (in red). The temperature evolution in the center of the vortex according to equation (1) is also drawn in black. (c) Temporal evolution of the SSH anomalies associated with A^{DW}. (d) Temporal evolution of the Rossby number associated with the dynamical core of the vortex C^{DW} (blue line), the vorticity (red line), and the strain (black line) associated with the external perturbations at 1500 m depth.

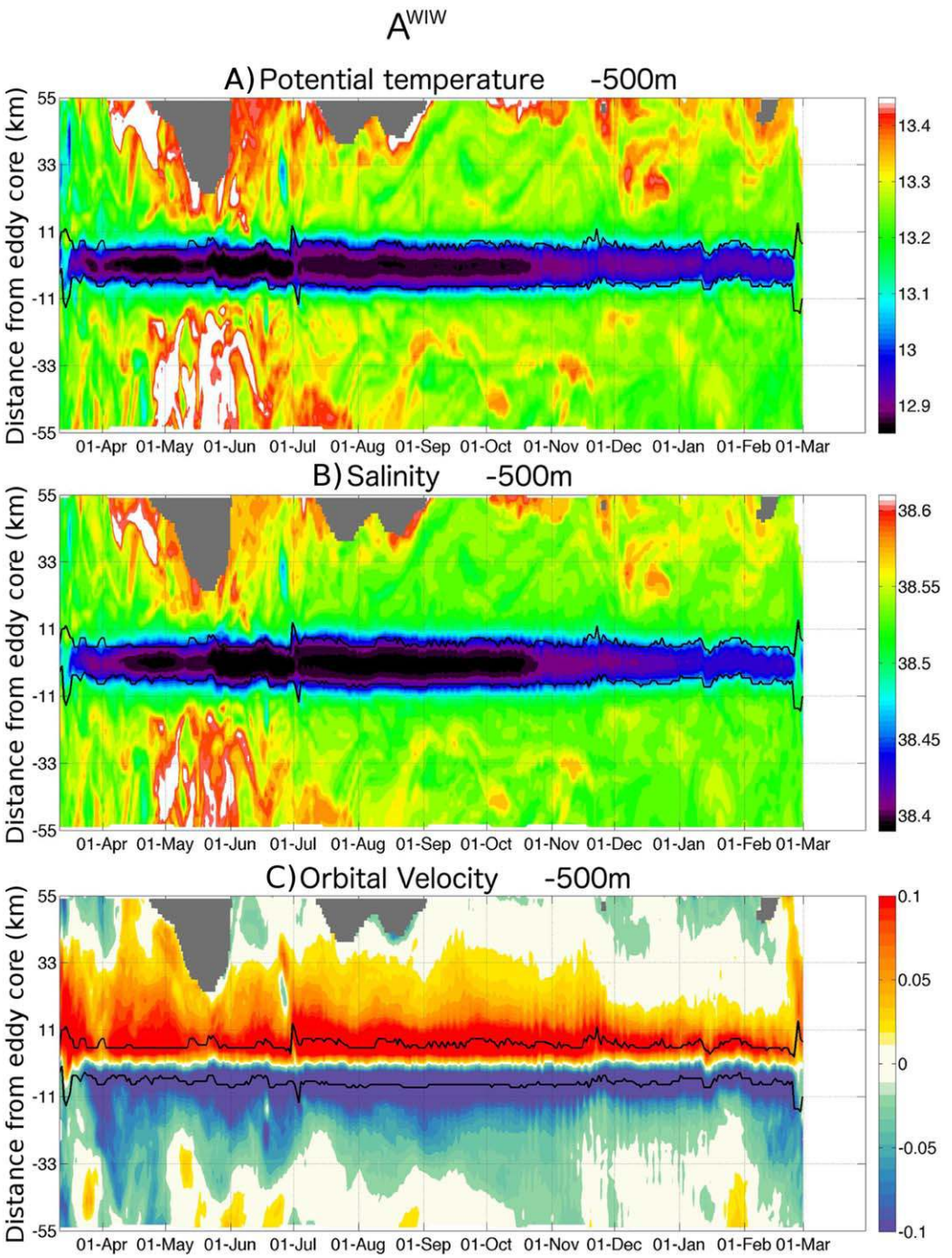

Figure 10. Same as Figure 8 for the anticyclonic SCV A^{wiw}. Hovmöller diagrams are calculated at 500 m depth.

observed at 1500 m depth. This is caused by the deepening of the eddy core until it reaches its depth of neutral buoyancy. After that, the core potential temperature decreases by only ∼0.02°C (Figure 8a) during its whole life, from ∼12.88°C to ∼12.86°C. Similarly, its core salinity decreases from 38.466 to 38.458 (Figure 8b). This slow decrease is correlated with a decrease of the T/S anomaly (Figure 9a) and reflects the diffusion processes resulting in the lateral mixing between the SCV and its surroundings. At 1500 m depth, the potential temperature anomaly also decreases, from ∼0.060°C to ∼0.031°C, and the salinity anomaly from ∼0.016 to ∼0.008.

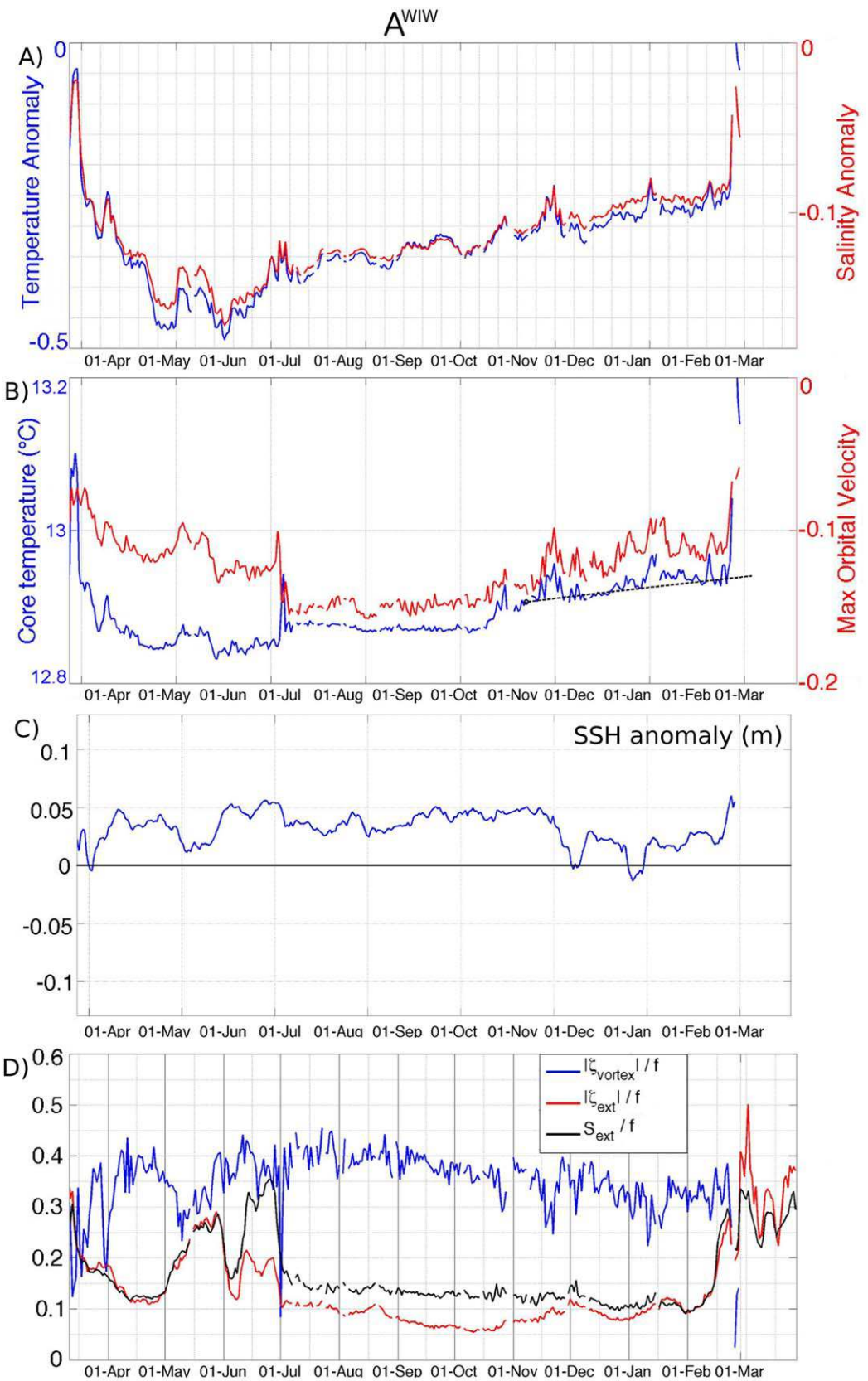

Figure 11. Same as Figure 9 for the anticyclonic SCV A^{WIW}. Temporal evolutions are calculated at 500 m depth.

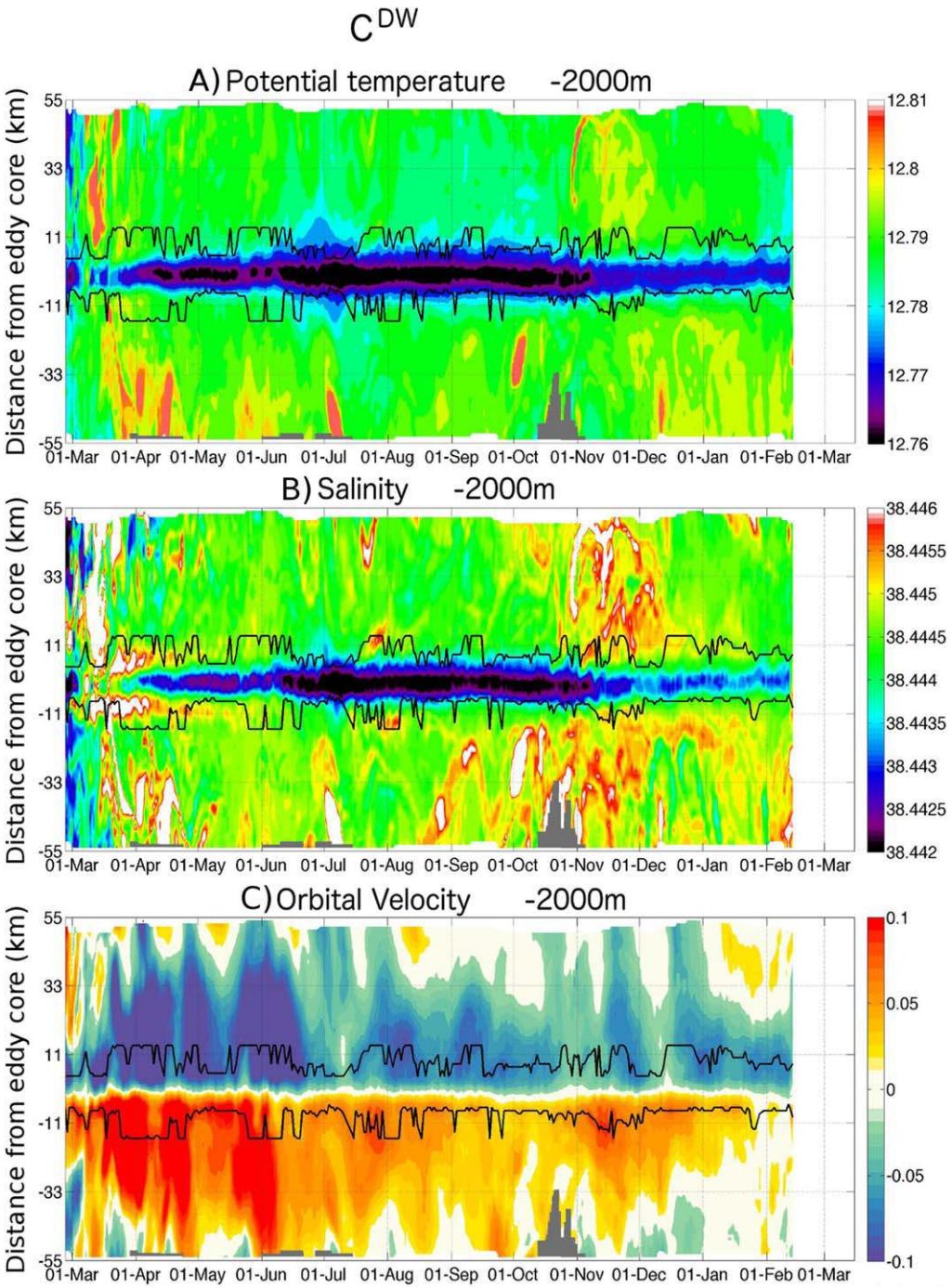

Figure 12. Same as Figure 8 for the cyclonic eddy C^{DW}. Hovmöller diagrams are calculated at 2000 m depth.

From March to October, the SCV radius remains stable at 6.5 km. A drastic decrease is observed in late October (from 6.5 to 4 km). This event is due to the interaction of the SCV with a larger mesoscale anticyclone (previously mentioned). This interaction implies a brief enhancement of the spreading of the vortex core characterized by a discontinuity in the evolution of the potential temperature at the center of the core (Figure 9b). Nevertheless, the SCV survives and its radius stabilizes at 4 km until it is destroyed 2.5 months later (about 11 months after its formation).

During the major part of its life, SCV A^{DW} has no surface signature. However, after 5 months, surface currents appear (visible on the time-averaged velocities of Figure 7.1c) and are associated with a positive SSH

anomaly of ∼+7 cm (see June 2009 on Figure 9c). This barotropization of the eddy could possibly result from its interaction with a surface-intensified anticyclone (not shown). We observe that these two surface and subsurface dynamical structures align along the same vertical. The surface component of the SCV A^{DW} vanishes after the interaction with the mesoscale anticyclone in October.

SCV A^{WIW} forms to the east of the convection zone on 11 March 2009 before being advected at a mean velocity of ∼2.6 cm/s for 350 days toward the north-west of Sardinia (Figure 1), where there is a strong northward flow mainly controlled by the Western Corsica Current [*Bosse et al*., 2015].

Like A^{DW}, A^{WIW} exhibits very good conservation of its thermohaline signature. The eddy forms in spring during the restratification phase following the winter deep convection event. When the MAW, which was destroyed by vertical mixing, covers the upper layers of the convection zone again, SCV A^{WIW} is pushed down and reaches its depth of neutral buoyancy around 500 m depth. This explains the decrease of the eddy potential temperature and salinity at 500 m depth observed from its formation to mid-May 2009 (Figures 10a and 10b). Afterwards, its core temperature increases by ∼0.1°C (Figure 10a) and its salinity by ∼0.05 (Figure 10b) over its lifetime of 9 months. During this period, the potential temperature anomaly evolves from ∼–0.45°C to ∼–0.23°C and the salinity anomaly from ∼–0.16 to ∼–0.08 (Figure 11a). This change is mainly driven by lateral diffusion of heat and salt from the warm, salty surrounding LIW layer.

Associated with the hydrographical transport, this structure has a surface signature (∼+4 cm of SSH on average) that persists during almost its whole lifetime (Figure 11c). Furthermore, a discontinuity can be seen in the core temperature and orbital velocities occurring in early July 2009 (Figure 11b). This results from the merging of the SCV A^{WIW} with another similar WIW SCV.

Figure 1 shows the trajectory of cyclone C^{DW}, which is advected by the large scale circulation at a mean velocity of 3.5 cm/s like the anticyclone A^{DW}. The cyclone also stays in the same area as the anticyclone, bounded to the south by the large mesoscale barotropic anticyclone and to the north and the west by the continental slope. The cyclone is dissipated 353 days after its formation (Movie S1 in the supporting information).

The evolution of the hydrographical core properties of the eddy C^{DW} is represented on Figure 12 at 2000 m depth, where its low stratified core is found. More precisely, the core evolution can be described in two chronological steps. The first phase lasts from the eddy formation on 25 February 2009 to early July 2009, when a diminution of the core temperature and salinity is observed. At 2000 m depth, the eddy potential temperature decreases from ∼12.78°C to ∼12.76°C (Figure 12a). During the same period, the salinity decreases from ∼38.444 to ∼38.442 (Figure 12b). The core evolution during this first phase can be translated as an increase of the potential temperature and salinity anomaly intensities: from ∼–0.005°C to ∼– 0.027°C for the temperature and from ∼0.001 to ∼–0.003 for the salinity (Figure 13a). During the second step, from early July 2009 to the destruction of the eddy in February 2010, the hydrographical eddy characteristics evolve in the sense opposite to the first phase. The potential temperature increases from ∼12.76°C to ∼12.77°C (Figure 12a) and the salinity from ∼38.442 to ∼38.444 (Figure 12b). This increase is also linked to a diminution of the hydrographical anomalies associated with the eddy core at 2000 m depth (Figure 13a).

In comparison with A^{DW}, C^{DW} quickly acquires an intense surface signature. During the first phase, a negative SSH anomaly reaches −14 cm at the end of May 2009 (Figure 13c). The isopycnal doming associated with the eddy intensifies, explaining the diminution of the potential temperature and salinity of the hydrographical core at 2000 m depth. The depth-averaged velocity is equal to ∼14 cm/s which is about 50% of V_{max} located near the surface (see Figure 14a for a typical eddy transect of the orbital velocity during this phase). In contrast, during the second stage of its life, the eddy C^{DW} tends to acquire a subsurface structure. A dynamical core associated with a maximum orbital velocity and stratification appears at about 250 m depth, far above the hydrographical core at the bottom of the ocean. The isopycnal doming slowly decreases, as does the SSH signature (from ∼–10 cm at the end of May 2009 to ∼–1 cm in October 2009). The depth-averaged currents of ∼ 8.5 cm/s represent 60% of the total orbital velocities. Figure 14b shows the eddy velocity structure during this second phase. The diminution of the hydrographical anomalies associated with the eddy C^{DW} through the second phase may be mainly caused by viscosity which decreases the intensity of orbital velocity (Figure 12c) and consequently the doming of isopycnals. Diffusive processes may also play a significant role. Note that the changes in its dynamical structure could have resulted from the interaction of C^{DW} with another cyclonic vortex. Similar subsurface small-scale cyclonic eddies have also

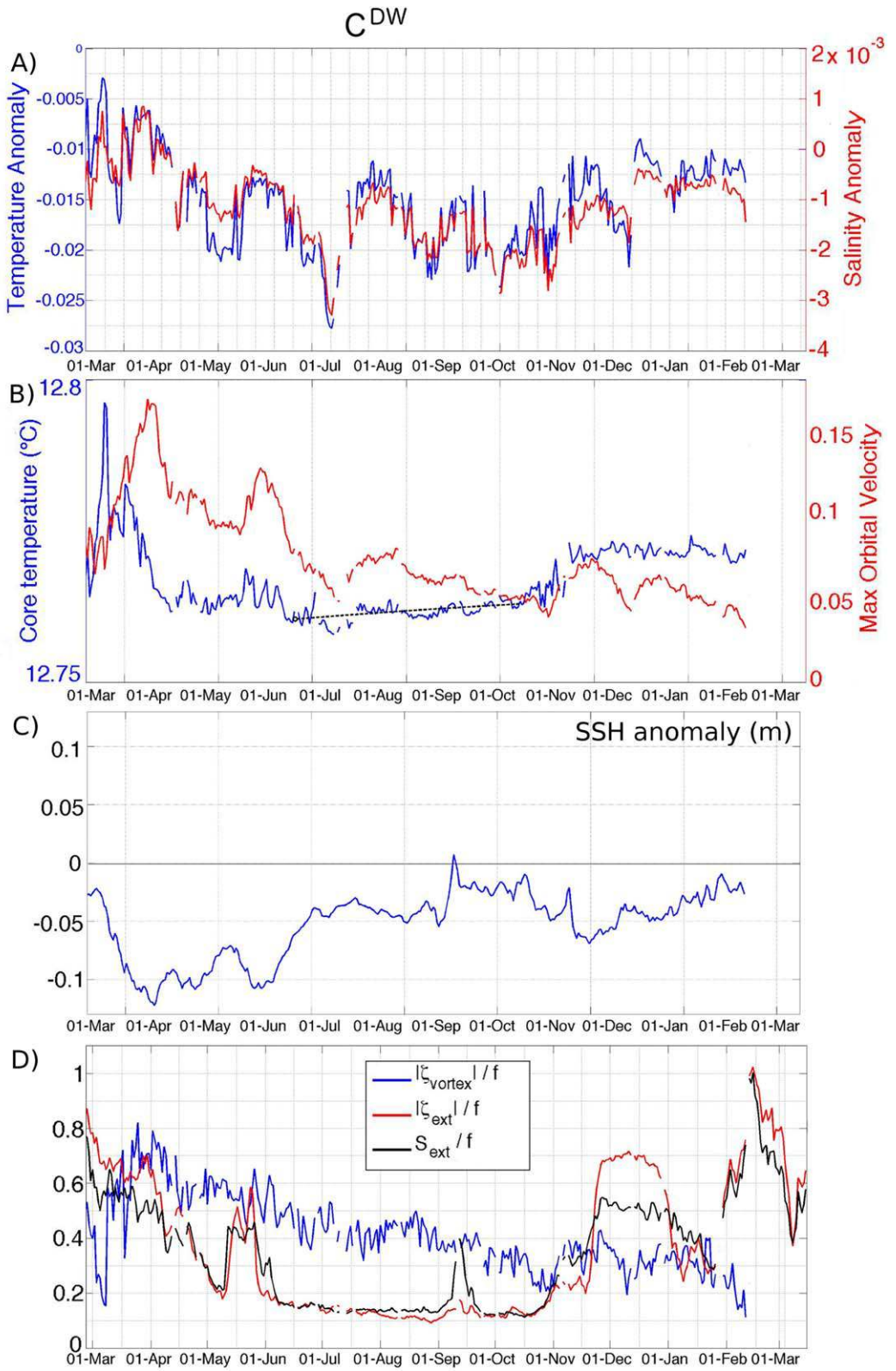

Figure 13. Same as Figure 9 for the cyclonic eddy C^{DW}. Temporal evolutions are calculated at 2000 m depth in Figures 13a and 13b and at 250 m depth in Figure 13d (depth of the dynamical core of C^{DW}).

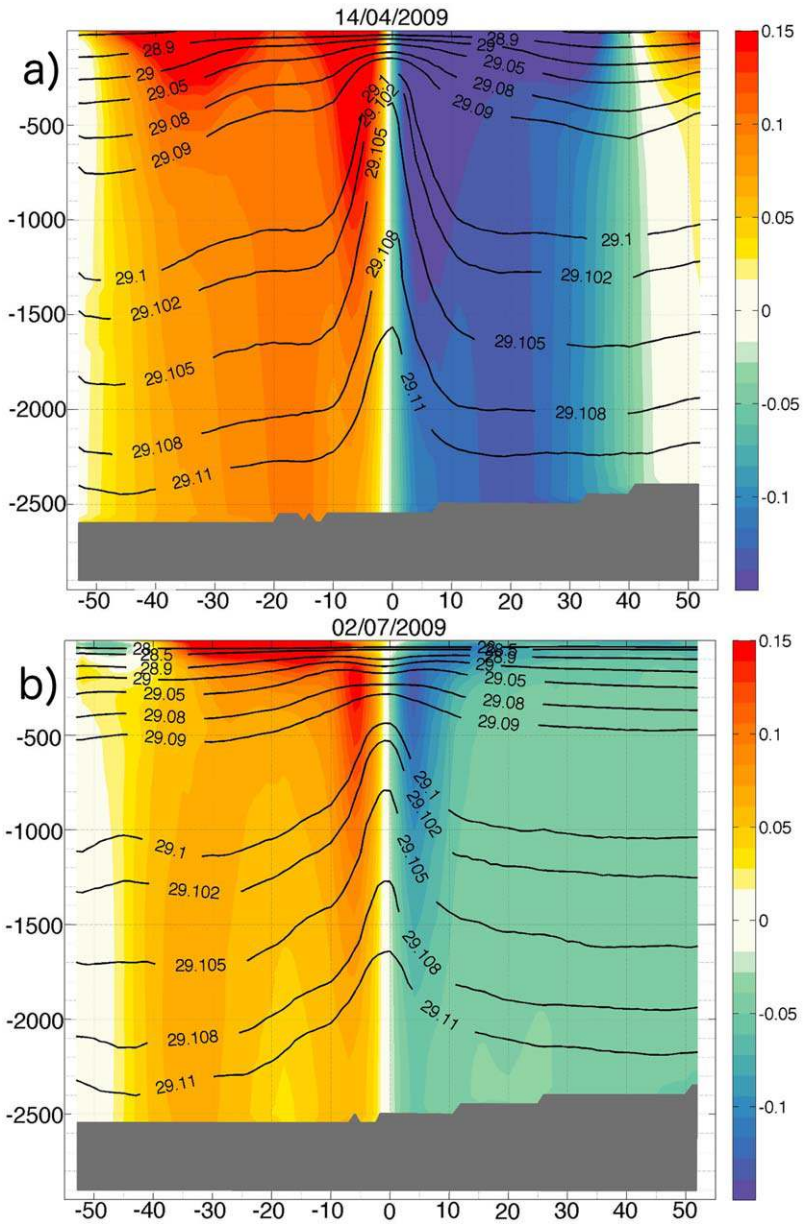

Figure 14. Transects across eddy C^{DW} of orbital velocity averaged over a week around (top) 14 April 2009 and (bottom) 02 July 2009. The black lines also show potential density anomaly contours and the gray shaded area indicates the seabed.

been described by *Bosse et al*. [2016] from in situ observations. They also pointed out that those structures, which have characteristics very similar to those of anticyclonic SCVs, could be considered as cyclonic SCVs even though the processes leading to the formation of such depth-intensified structures still needs to be more thoroughly investigated.

A sudden increase of the core potential temperature and salinity can also be observed in November 2009. This happens when the SCV C^{DW} approaches the continental slope (Figure 12) and interacts with the warm, salty Northern Current, resulting in a sudden increase of the heat/salt diffusion toward the C^{DW} core.

4.3. Diffusive Processes Affecting SCVs

The simulated SCV lifetimes are about 1 year and, during this time, they transport waters with particular characteristics along their pathway. Oceanic tracers embedded within such structures are carried from their generation to their destruction site with very little alteration. These eddies can thus be particularly effective in transporting physical and biogeochemical tracers over long periods of time and long distances.

Nevertheless, the hydrographical anomalies associated with SCVs tend to decrease throughout the lifetime of the structures. This decay results from two kinds of processes: interactions with external flows having typical sizes of the order of the SCV size or larger, and diffusive processes including effective diffusion and interaction with scales smaller than the SCVs. The former potentially induce a brief and intense degradation of the core while the latter produce a slow dissipation of the vortex core.

Under the action of the diffusive processes, the decay of the SCV T/S anomaly may follow the heat equation (assuming an isolated vortex subjected only to horizontal diffusion) expressed basically in a unidimensional Cartesian coordinate system as

$$\frac{\partial T}{\partial t} = \kappa_h \frac{\partial^2 T}{\partial x^2}, \tag{1}$$

where T is the potential temperature, t the time, and κ_h the horizontal diffusion coefficient. To estimate κ_h for the simulated SCVs (A^{DW}, A^{WIW} and C^{DW}), a minimum period of 4 months is chosen during which the vortex is not in interaction with strong external flows ($S_{ext.} < \zeta_{vortex}$ and $\zeta_{ext.} < \zeta_{vortex}$, see section 4.4). Then, starting from a radial distribution of temperature corresponding to the beginning of the period for each SCV, it is allowed to evolve according to (1). We then search for the constant horizontal diffusion κ_h that fits the potential temperature evolution in the SCV core (see dashed lines in Figures 9b, 11b, and 13b). For A^{DW}, A^{WIW}, and C^{DW} respectively, κ_h is found to be equal to 0.64, 0.55, and 0.23 m^2/s. A typical time scale (R^2/κ_h) can be associated with this diffusion coefficient and corresponds to a typical lifetime of an SCV decaying only by diffusion (in the absence of external interactions with other flows having typical sizes of the order of the SCV or larger). We obtained $\sim$2.1 years for A^{DW}, 3.2 years for A^{WIW}, and 5.1 years for C^{DW}, suggesting that diffusion might act on a longer time scale than the seasonal forcing. Winter vertical mixing might hence be an important source of perturbation for SCV dissipation.

The values found for κ_h are low compared to the estimations made by *McWilliams* [1985] for the Atlantic "Meddies" ($\sim$20 m^2/s), mainly because our calculation does not take interactions with energetic flows into account. However, *Ruddick and Herbert* [1988] have shown that lateral exchanges of a Meddy with its surroundings are consistent with a radial diffusivity of $\sim$0.4 m^2/s. The present results are in good agreement with this estimation. Finally, as the SCV's radius is rather stable during its lifetime, the decay of the T/S anomaly implies heat/salt exchanges between the SCV and its surrounding waters all along their pathway.

The diffusive mechanisms of SCVs have been investigated in several studies, mainly based on the Meddies observed in the North Atlantic. *Ruddick and Herbert* [1988] show that thermohaline intrusions are the dominant mechanism for mixing Mediterranean salt lenses. Evidence of erosion by lateral intrusive motions and vertical mixing have been found in the upper and lower part of SCVs caused by double-diffusive convection and salt-fingers sometimes called layering [*Armi et al*., 1989; *Ruddick*, 1992; *Hua et al*., 2013]. *Paldor* [1999] explains that long-lived vortices such as SCVs are highly unstable with respect to small-scale perturbations because of the PV discontinuity at the edge of the eddy. Hence, this unstable tendency tends to decrease with time as diffusion processes smooth the jump of PV.

4.4. Cohesion or Destruction of SCVs in Interaction With External Flows

Along their pathway in the northwestern Mediterranean Sea, the simulated SCVs interact with other oceanic structures. Those mechanisms eventually destabilize the vortex and affect its longevity. *Provenzale* [1999] has demonstrated the strong impermeability to inward and outward fluxes associated with vortices by using simulations of Lagrangian virtual particles. Nonetheless, this author notes that particles eventually migrate between the core of an eddy and its surroundings when highly dissipative events (e.g., strong interactions with external flows) lead to the vortex deformation and to the formation of filaments. *McWilliams* [1985] also suggested that a SCV could survive interactions with other flows if its vorticity dominates the background vorticity and strain fields. According to this suggestion, the cohesion of an SCV resides in the intensity of its vorticity $|\zeta|$ (i.e., in its Rossby number R_o). Figures 8c, 10c, and 12c show how, by smoothing the density gradients of the simulated eddies, diffusion processes also induce a decay of the SCV's kinetic energy. The decrease of the orbital velocity by about 1 cm/s per month during the SCV lifetime is noticeable for the three studied eddies (Figures 9b, 11b, and 13b). Given that their radius remains almost constant, their Rossby number progressively decreases. For A^{DW}, the Rossby number peaks at $\sim$0.5 after its formation and decreases to $\sim$0.2 before its destruction (Figure 9d). The same behavior is also observed for A^{WIW} with

a Rossby number decreasing from ~0.45 to ~0.3 (Figure 11d) and for C^{DW}, with an R_o decreasing from ~0.6 to ~0.25 (Figure 13d). Consequently, SCVs become less and less resistant to external perturbations.

The external flow in the surroundings of each SCV can be characterized by its horizontal strain and relative vorticity. Normalized by the Coriolis parameter, these can be written:

$$|S|/f = \sqrt{(\partial u/\partial x - \partial v/\partial y)^2 + (\partial v/\partial x + \partial u/\partial y)^2}/f, \quad (2)$$

$$|\zeta|/f = \sqrt{(\partial v/\partial x - \partial u/\partial y)^2}/f. \quad (3)$$

At each time step, the strain and vorticity fields are computed in a region 10–50 km from the SCV center position and the depth of its dynamical core (i.e., −1500 m for A^{DW}, −500 m for A^{WIW}, and −250 m for C^{DW}). Hypothesizing that the structures perturbing the SCV are associated with the highest values in that region, we quantify the $S_{ext.}$ and $\zeta_{ext.}$ associated with external perturbations as the average of the values above the 95th percentile of the strain and vorticity distributions in the vicinity of each SCV. The evolutions of the Rossby numbers of the SCVs are represented together with $S_{ext.}$ and $\zeta_{ext.}$ in Figures 9d, 11d, and 13d for A^{DW}, A^{WIW}, and C^{DW}, respectively.

Globally, the SCV's Rossby number is usually greater than the external strain and vorticity. This confirms that the vortices most often evolve without interaction with external perturbations and are mainly subject to slow diffusive mixing processes. However, during some particular events, the external strain and vorticity reach values similar to those of the SCVs or even exceed them. We can distinguish three categories of interactions. The first one induces increased fading of the SCV's core properties without affecting its dynamical structure. Such interactions are observable for A^{DW} at the beginning of May 2009 and for C^{DW} at the end of May 2009. This first event is due to the interaction with the continental slope and the slope current, while the second one happens in the vicinity of a mesoscale anticyclone. This second class of interactions results in a drastic alteration of the SCV's dynamical structure. For instance, a strong diminution of A^{DW} radius occurs in late October 2009 (from 6.5 to 4 km). This event is due to its interaction with a mesoscale anticyclone (radius ~ 50 km) characterized by comparable relative vorticity ($\zeta = 0.32f$). The mesoscale anticyclone thus alters the dynamical structure of the SCV, which is nevertheless able to survive. The decrease of the SCV radius leads to an increase of the Rossby number from 0.15 to 0.25. This mesoscale anticyclone is also located in the vicinity of C^{DW} from November to December 2016, causing a marked increase in the core potential temperature (of ~0.01°C at 2000 m, Figure 13b). For these two kinds of interactions, the external strain and vorticity are usually close to those of the SCV Rossby number. Finally, there are interactions leading to the destruction of the SCVs. For the three long-lived vortices considered here, such interactions only occurred when the horizontal currents became much more energetic in response to the initiation of the following convective event of winter 2009–2010. If they are present in the convective zone about 1 year after their formation, the SCVs are not able to survive deep vertical mixing and the associated strong horizontal shear and strain. The simulated strain and vorticity of the ambient field indeed reached large values during this period (~0.5f). The result of an SCVs destruction is of course that the water mass trapped in their core is released, thus participating in the spreading of the convected waters, potentially to large distances from the formation site and with a delay comparable to that of dense water transported by mesoscale eddies or directly drained into the boundary current.

5. Spreading of Newly Formed Waters by Anticyclonic SCVs and Local Preconditioning

Submesoscale coherent eddies are known to participate significantly in the large scale spreading of the nWMDW toward the whole Western Mediterranean Sea [*Testor and Gascard*, 2006]. We can use our simulation to estimate this contribution. First, the volume of nWMDW formed by winter vertical mixing can be estimated as the volume crossing the 29.1 kg m^{-3} isopycnal due to air-sea buoyancy fluxes using the method of *Walin* [1982] as done by *Speer and Tziperman* [1992] and *Herrmann et al*. [2008]. This corresponds to a total volume of 4830 km^3 for the winter of 2008–2009. At the end of this convective event, at least four additional anticyclonic SCVs comparable to the A^{DW} studied above (Figure 3.4b) can be identified. We estimate that the anticyclonic SCV A^{DW} traps about 157 km^3 of nWMDW in its core, corresponding to ~3.25%

of the total production. Considering the five anticyclonic SCVs detected by the eddy tracking algorithm just after the convective event, it is expected that ∼15% of the nWMDW would be exported out of the deep water formation zone by such anticyclonic submesoscale eddies.

The volume of WIW formed during winter 2008–2009 is estimated using the criterion $T < 12.9°C$ and $S < 38.4$. From this estimation made at the end of the convection, we subtract the volume of WIW present in the convection area just before the deepening of the mixed layer. Only WIW that has been isolated from atmospheric fluxes by surface restratification or subduction is taken into account. This corresponds to a volume of 4800 km^3. The typical SCV A^{WIW} contains a volume of about 91 km^3, corresponding to ∼1.90% of the total WIW production. Twenty vortices similar to A^{WIW} are also tracked in February 2009, 10 of them having a lifetime that exceeds one month. Most of them are destroyed by the interaction with the Northern Current or with other intense dynamical structures found in the convection zone. Considering the 20 SCVs detected, it is deduced that SCVs can be responsible for the spreading of at least ∼35% of the total WIW export out of the convection zone.

We find similar results for the anticyclonic SCVs of nWMDW and WIW formed during the convection event of the following winter 2009–2010. It is worth emphasizing that the eddy tracking algorithm could have failed to detect some short-lived eddies. So, the estimated 15% (respectively 35%) is probably a lower bound for the proportion of nWMDW (resp. WIW) transported within such coherent eddies. This estimation is however in good agreement with the findings of *Testor and Gascard* [2006] who calculate that each SCV is responsible for the export of ∼1% of the newly formed waters and, *Bosse et al*. [2016] who evaluate their overall transport as 20–35% of the total volume exported.

Moreover, *Testor and Gascard* [2006] and *Bosse et al*. [2016] reveal the presence of small-scale cyclonic eddies having a core of typical nWMDW formed during a convective winter. Their generation would be favored by a mixed layer that reaches the bottom and so by a very intense convective winter. The convective event simulated in this study may not be deep enough to create the conditions for the generation of such cyclones. Indeed, C^{DW} is distinct since it does not participate in the spreading of deep waters. On the contrary, its strong stratified subsurface core makes it more likely to be involved in the restratification process. Four more cyclonic vortices similar to C^{DW} are also formed after the convective event and tracked by the algorithm. Their generation appears to be closely linked with the anticyclonic SCVs having a nWMDW core since they are generated at the same time. Their radius ranges between 5.5 and 6.5 km and their orbital velocities between 5.9 and 11.8 cm/s.

Lherminier et al. [1999] and *Budéus et al*. [2004] suggest that eddies present in the convection zone could be preferential spots for the initiation of deep convection the following winter. Based on the average density section of Figure 7, the preconditioning effect of the anticyclonic SCV A^{DW} (respectively cyclonic SCV C^{DW}) can be estimated by computing the columnar buoyancy at 2000 m depth [*Herrmann et al*., 2008] which corresponds to the buoyancy loss required to mix the initially stratified water column down to 2000 m. Compared to the surroundings, a decrease of 2.5% (resp. 12.1%) of the columnar buoyancy is found within the core of the anticyclonic SCV (resp. cyclonic SCV). This difference represents a 1000 W/m^2 surface heat flux lasting for about 1 day, corresponding to an intense cooling event. In conclusion, SCVs could have an impact on the depth reached by the mixed layer in winter through the local preconditioning they generate.

6. Conclusions and Perspectives

This study presents the results of the first realistic numerical regional simulation able to generate submesoscale coherent vortices (SCVs) having a lifetime of several months in a region of open ocean deep convection. Their formation is associated with convective events and the instability of the front bounding the mixed patch. Anticyclonic SCVs are generated by the dynamical adjustment of mixed waters introduced into the stratified environment, when convection has still not reached the bottom. Having a core of newly formed waters, anticyclonic SCVs participate actively in their spreading. The generation of cyclonic eddies is closely linked to the anticyclones as they are probably the cyclonic components of dipolar structures that form at the rim of the convection area. These cyclonic SCVs are more likely to be involved in the restratification process.

The simulation performed allows the role of anticyclonic SCVs in the transport of the newly formed water to be quantified. It has been found that they are responsible for the export of about 15% of the newly formed deep waters and 35% of the WIW over large distances (hundreds of kilometers) and during long periods of time. We quantify their lateral diffusion coefficient as close to 0.2–0.6 m^2/s. Their resistance to external perturbations is due to their strong nonlinearity (Rossby number larger than 0.1) compared to the vorticity and strain of the surrounding flow. Despite their small size, they have a great impact on the ventilation and dispersion of deep waters. The simulated SCVs are advected throughout the model domain for several months or even up to 1 year, until they collapse. This is consistent with the observations of *Testor and Gascard* [2003] who report eddies drifting southward and reaching the Algerian basin. A larger numerical domain extending to the southern basin with the same very high resolution would be required to simulate this effect in a convenient way. Because of their small radius (of about 5 km), a very high resolution (at least 1 km) is required to represent them. This is an issue for climate models that do not have the appropriate grid resolution but do strongly need to simulate the ventilation processes of the ocean properly.

A first step towards parametrization of these processes could be to use a two-way nesting approach with a very high-resolution model for the deep convection area embedded in a coarser model. This would allow the integral effects of deep convection to be compared with a twin, but low resolution and interannual simulation. However, sensitivity studies are necessary to address this point, as care must be taken with the domain definitions. Even if the high-resolution nested model is able to create SCVs, they will dissipate artificially as soon as they are advected into the coarser resolution model. Their dynamical role could thus be largely distorted. The high-resolution nested domain would need to be large enough to fully represent the deep convection phenomena and the spreading of SCVs as far as necessary, to avoid erroneous conclusions.

Acknowledgments
We thank Beuvier and Mercator Ocean for NemoMed12 model outputs, Somot and Météo-France for Aladin model outputs, and Nencioli for providing the eddy detection and tracking algorithm. We also thank two anonymous reviewers for their constructive comments and suggestions which helped improve this manuscript. This study was supported by ANR-11-MONU-005 (COMODO), ANR-12-BS06-0003 (Asics-Med), and the PERSEUS project (European Union FP7 grant agreement 287600). It is a contribution to the HyMeX (Hydrological cycle in the Mediterranean Experiment) and MerMex (Marine Ecosystem Response in the Mediterranean Experiment) projects of the MISTRALS international program. Numerical simulations were performed using HPC resources from CALMIP (grants P09115 and P1325) and the Laboratoire d'Aérologie cluster. The SYMPHONIE ocean model is developed by the SIROCCO group and its sources are available at http://sirocco.omp.obs-mip.fr/ocean_models/S-model/download. Model outputs used in this study can be requested at sirocco@aero.obs-mip.fr.

References

Akitomo, K. (2010), Baroclinic instability and submesoscale eddy formation in weakly stratified oceans under cooling, *J. Geophys. Res.*, *115*, C11027, doi:10.1029/2010JC006125.

Allen, J. T., S. C. Painter, and M. Rixen, (2008), Eddy transport of Western Mediterranean Intermediate Water to the Alboran Sea, *J. Geophys. Res.*, *113*, C04024, doi:10.1029/2007JC004649.

Armi, L., D. Herbert, N. Oakey, J. Price, P. L. Richardson, T. Rossby, and B. A. Ruddick (1988), The history and decay of a Mediterranean salt lens, *Nature*, *333*, 649–651, doi:10.1038/333649a0.

Armi, L., D. Herbert, N. Oakey, J. Price, P. L. Richardson, T. Rossby, and B. A. Ruddick (1989), Two years in the life of a Mediterranean salt lens, *J. Phys. Oceanogr.*, *19*, 354–370, doi:10.1175/1520-0485(1989)019 < 0354:TYITLO>2.0.CO;2.

Barbosa Aguiar, A. C., A. Peliz, and X. Carton (2013), A census of Meddies in a long-term high-resolution simulation, *Prog. Oceanogr.*, *116*, 80–94, doi:10.1016/j.pocean.2013.06.016.

Beuvier, J., K. Beranger, C. Lebeaupin Brossier, S. Somot, F. Sevault, Y. Drillet, R. Bourdalle-Badie, N. Ferry, and F. Lyard (2012), Spreading of the Western Mediterranean Deep Water after winter 2005: Time scales and deep cyclone transport, *J. Geophys. Res.*, *117*, C07022, doi:10.1029/2011JC007679.

Bosse, A., P. Testor, L. Mortier, L. Prieur, V. Taillandier, F. D'Ortenzio, and L. Coppola (2015), Spreading of Levantine Intermediate Waters by submesoscale coherent vortices in the northwestern Mediterranean Sea as observed with gliders, *J. Geophys. Res. Oceans*, *120*, 1599–1622, doi:10.1002/2014JC010263.

Bosse, A., et al. (2016), Scales and dynamics of submesoscale coherent vortices formed by deep convection in the northwestern Mediterranean Sea, *J. Geophys. Res. Oceans*, *121*, 7716–7742, doi:10.1002/2016JC012144.

Budéus, G., B. Cisewski, S. Ronski, D. Dietrich, and M. Weitere (2004), Structure and effects of a long lived vortex in the Greenland Sea, *Geophys. Res. Lett.*, *31*, L05304, doi:10.1029/2003GL017983.

Dong, C., X. Lin, Y. Liu, F. Nencioli, Y. Chao, Y. Guan, D. Chen, T. Dickey, and J. C. McWilliams (2012), Three-dimensional oceanic eddy analysis in the Southern California Bight from a numerical product, *J. Geophys. Res.*, *117*, C00H14, doi:10.1029/2011JC007354.

Durrieu de Madron, X., et al. (2013), Interaction of dense shelf water cascading and open-sea convection in the northwestern Mediterranean during winter 2012, *Geophys. Res. Lett.*, *40*, 1379–1385, doi:10.1002/grl.50331.

Ertel, H., and C. G. Rossby (1949), A new conservation theorem of hydrodynamics, *Geofis. pura appl.*, *14*, 189–193.

Estournel, C., and D. Guedalia (1987), A new parameterization of eddy diffusivities for nocturnal boundary-layer modelling, *Boundary Layer Meteorol.*, *39*, 191–203, doi:10.1007/BF00121874.

Estournel, C., F. Auclair, M. Lux, C. Nguyen, and P. Marsaleix, (2009), "Scale oriented" embedded modeling of the North-Western Mediterranean in the frame of MFSTEP, *Ocean Sci.*, *5*, 73–90, doi:10.5194/os-5-73-2009.

Estournel, C., et al. (2016), High resolution modeling of dense water formation in the north-western Mediterranean during winter 2012–2013: Processes and budget, *J. Geophys. Res. Oceans*, *121*, 5367–5392, doi:10.1002/2016JC011935.

Gascard, J.-C. (1978), Mediterranean deep water formation baroclinic instability and oceanic eddies, *Oceanol. Acta*, *1*, 315–330.

Gascard, J.-C., and R. A. Clarke (1983), The formation of Labrador Sea water. Part II: Mesoscale and smaller-scale processes, *J. Phys. Oceanogr.*, *13*(10), 1779–1797, doi:10.1175/1520-0485(1983)013 < 1779:TFOLSW>2.0.CO;2.

Gascard, J.-C., A. J. Watson, M.-J. Messias, K. A. Olsson, T. Johannessen, and K. Simonsen (2002), Long-lived vortices as a mode of deep ventilation in the Greenland Sea, *Nature*, *416*, 525–527, doi:10.1038/416525a.

Gasparini, G., G. Zodiatis, M. Astraldi, C. Galli, and S. Sparnocchia (1999), Winter intermediate water lenses in the Ligurian Sea, *J. Mar. Sys.*, *20*(1–4), 319–332, doi:10.1016/S0924-7963(98)00089-X.

Griffies, S., and R. Hallberg (2000), Biharmonic friction with a Smagorinsky-like viscosity for use in large-scale eddy-permitting ocean models, *Mon. Weather Rev.*, *128*(8), 2935–2946, doi:10.1175/1520-0493(2000)128 < 2935:BFWASL>2.0.CO;2.

Herrmann, M., S. Somot, F. Sevault, C. Estournel, and M. Déqué (2008), Modeling the deep convection in the northwestern Mediterranean Sea using an eddy-permitting and an eddy-resolving model: Case study of winter 1986–1987, *J. Geophys. Res.*, *113*, C04011, doi:10.1029/2006JC003991.

Herrmann, M., S. Somot, S. Calmanti, C. Dubois, and F. Sevault (2011), Representation of spatial and temporal variability of daily wind speed and of intense wind events over the Mediterranean Sea using dynamical downscaling: Impact of the regional climate model configuration, *Nat. Hazards Earth Syst. Sci.*, *11*(7), 1983–2001, doi:10.5194/nhess-11-1983-2011.

Houpert, L., et al. (2016), Observations of open-ocean deep convection in the northwestern Mediterranean Sea: Seasonal and interannual variability of mixing and deep water masses for the 2007–2013 period, *J. Geophys. Res. Oceans*, *121*, 8139–8171, doi:10.1002/2016JC011857.

Hua, B. L., C. Ménesguen, S. Le Gentil, R. Schopp, B. Marsset, and H. Aiki, (2013), Layering and turbulence surrounding an anticyclonic oceanic vortex: In situ observations and quasi-geostrophic numerical simulations, *J. Fluid Mech.*, *731*, 418–442, *doi*:10.1017/jfm.2013.369.

Jackett, D. R., T. J. McDougall, R. Feistel, D. G. Wright, and S. M. Griffies (2006), Algorithms for density, potential temperature, conservative temperature, and the freezing temperature of seawater, *J. Atmos. Oceanic Technol.*, *23*, 1709–1728, doi:10.1175/JTECH1946.1.

Jones, H., and J. Marshall (1993), Convection with rotation in a neutral ocean: A study of open-ocean deep convection, *J. Phys. Oceanogr.*, *23*, 1009–1039, doi:10.1175/1520-0485(1993)023 < 1009:CWRIAN>2.0.CO;2.

Lee, M. M., A. C. Coward, and A. G. Nurser (2002), Spurious diapycnal mixing of the deep waters in an eddy-permitting global ocean model, *J. Phys. Oceanogr.*, *32*(5), 1522–1535, doi:10.1175/1520-0485(2002)032 < 1522:SDMOTD>2.0.CO;2.

Legg, S., and J. C. Marshall (1993), A heton model of the spreading phase of open-ocean deep convection, *J. Phys. Oceanogr.*, *23*(6), 1040–1056, doi:10.1175/1520-0485(1993)0232.0.CO;2.

Legg, S., H. Jones, and M. Visbeck (1996), A heton perspective of baroclinic eddy transfer in localized ocean convection, *J. Phys. Oceanogr.*, *26*, 2251–2266, doi:10.1175/1520-0485(1996)026 < 2251:AHPOBE>2.0.CO;2.

Lherminier, P., J.-C. Gascard, and D. Quadfasel (1999), The Greenland Sea in winter 1993 and 1994: Preconditioning for deep convection, *Deep Sea Res., Part II*, *46*, 1199–1235, doi:10.1016/S0967-0645(99)00020-X.

Lilly, J. M., P. B. Rhines, F. Schott, K. Lavender, J. Lazier, U. Send, and E. D'Asaro (2003), Observations of the Labrador Sea eddy field, *Prog. Oceanogr.*, *59*, 75–176, doi:10.1016/j.pocean.2003.08.013.

Marchesiello, P., L. Debreu, and X. Couvelard, (2009), Spurious diapycnal mixing in terrain-following coordinate models: The problem and a solution, *Ocean Modell.*, *26*, 156–169, doi:10.1016/j.ocemod.2008.09.004.

Marsaleix, P., F. Auclair, and C. Estournel (2006), Considerations on open boundary conditions for regional and coastal ocean models, *Atmos. Oceanic Technol.*, *23*, 1603–1613, doi:10.1175/JTECH1930.1.

Marsaleix, P., F. Auclair, J. W. Floor, M. J. Herrmann, C. Estournel, I. Pairaud, and C. Ulses (2008), Energy conservation issues in sigma-coordinate free-surface ocean models, *Ocean Modell.*, *20*, 61–89, doi:10.1016/j.ocemod.2007.07.005.

Marsaleix, P., F. Auclair, and C. Estournel (2009), Low-order pressure gradient schemes in sigma coordinate models: The seamount test revisited, *Ocean Modell.*, *30*(2–3), 169–177, doi:10.1016/j.ocemod.2009.06.011.

Marsaleix, P., F. Auclair, C. Estournel, C. Nguyen, and C. Ulses (2011), An accurate implementation of the compressibility terms in the equation of state in a low order pressure gradient scheme for sigma coordinate ocean models, *Ocean Modell.*, *40*(1), 1–13, doi:10.1016/j.ocemod.2011.07.004.

Marsaleix, P., F. Auclair, T. Duhaut, C. Estournel, C. Nguyen, and C. Ulses (2012), Alternatives to the Robert-Asselin filter, *Ocean Modell.*, *41*, 53–66, doi:10.1016/j.ocemod.2011.11.002.

Marshall, J., and F. Schott (1999), Open-ocean convection: Observations, theory, and models, *Rev. Geophys.*, *37*, 1–64, doi:10.1029/98RG02739.

McWilliams, J. C. (1985), Submesoscale, coherent vortices in the ocean, *Rev. Geophys.*, *23*, 165–182, doi:10.1029/RG023i002p00165.

McWilliams, J. C. (1988), Vortex generation through balanced adjustment, *J. Phys. Oceanogr.*, *18*, 1178–1192, doi:10.1175/1520-0485(1988)018 <1178:VGTBA>2.0.CO;2.

MEDOC-Group (1970), Observation of formation of deep water in the Mediterranean Sea, 1969, *Nature*, *225*, 1037–1040, doi:10.1038/2271037a0.

Mertens, C., and F. Schott (1998), Interannual variability of deep-water formation in the northwestern Mediterranean, *J. Phys. Oceanogr.*, *28*(7), 1410–1424, doi:10.1175/1520-0485(1998)028 < 1410:IVODWF>2.0.CO;2.

Michaud, H., P. Marsaleix, Y. Leredde, C. Estournel, F. Bourrin, F. Lyard, C. Mayet, and F. Ardhuin (2012), Three-dimensional modelling of wave-induced current from the surf zone to the inner shelf, *Ocean Sci.*, *8*, 657–681, doi:10.5194/os-8-657-2012.

Millot, C. (1999), Circulation in the western Mediterranean sea, *J. Mar. Syst.*, *20*, 423–442, doi:10.1016/S0924-7963(98)00078-5.

Narimousa, S. (1998), Turbulent convection into a linearly stratified fluid: The generation of 'subsurface anticyclones', *J. Fluid Mech.*, *354*, 101–121, doi:10.1017/S002211209700743X.

Nencioli, F., C. Dong, T. Dickey, L. Washburn, and J. C. McWilliams (2010), A vector geometry-based eddy detection algorithm and its application to a high-resolution numerical model product and high-frequency radar surface velocities in the Southern California Bight, *J. Atmos. Oceanic Technol.*, *27*, 564–579, doi:10.1175/2009JTECHO725.1.

Oliver, K. I. C., T. Eldevik, D. P. Stevens, and A. J. Watson (2008), A Greenland Sea perspective on the dynamics of postconvective eddies, *J. Phys. Oceanogr.*, *38*(12), 2755–2771, doi:10.1175/2008JPO3844.1.

Paldor, N. (1999), Linear instability of barotropic submesoscale coherent vortices observed in the ocean, *J. Phys. Oceanogr.*, *29*, 1442–1452, doi:10.1175/1520-0485(1999)029 < 1442:LIOBSC>2.0.CO;2.

Petrenko, A., C. Dufau, and C. Estournel (2008), Barotropic eastward currents in the western Gulf of Lion, north-western Mediterranean Sea, during stratified conditions, *J. Mar. Syst.*, *74*, 406–428, doi:10.1016/j.jmarsys.2008.03.

Pickart, R. S., W. M. Smethie, J. R. Lazier, E. P. Jones, and W. J. Jenkins (1996), Eddies of newly formed upper Labrador Sea water, *J. Geophys. Res.*, *399*, 20,711–20,726, doi:10.1029/96JC01453.

Pinot, J. M., and A. Ganachaud (1999), The role of Winter Intermediate Waters in the spring-summer circulation of the Balearic Sea: 1. Hydrography and inverse modelling, *J. Geophys. Res.*, *104*, 29,843–29,864, doi:10.1029/1999JC900202.

Provenzale, A. (1999), Transport by coherent barotropic vortices, *Ann. Rev. Fluid Mech.*, *31*, 55–93, doi:10.1146/annurev.fluid.31.1.55.

Rixen, M., et al. (2005), The Western Mediterranean Deep Water: A proxy for climate change, *Geophys. Res. Lett.*, *32*, L12608, doi:10.1029/2005GL022702.

Ronski, S., and G. Budéus (2006), Vertical structure reveals eddy lifetime in the Greenland Sea, *Geophys. Res. Lett.*, *33*, L11602, doi:10.1029/2006GL026045.

Rubio, A., B. Barnier, G. Jorda, M. Espino, and P. Marsaleix, (2009), Origin and dynamics of mesoscale eddies in the Catalan Sea (NW Mediterranean): Insight from a numerical model study, *J. Geophys. Res.*, *114*, C06009, doi:10.1029/2007JC004245.

Ruddick, B. (1992), Intrusive mixing in a Mediterranean salt lens—Intrusion slopes and dynamical mechanisms, *J. Phys. Oceanogr.*, *22*(11), 1274–1285, doi:10.1175/1520-0485(1992)022 < 1274:IMIAMS>2.0.CO;2.

Ruddick, B., and D. Herbert (1988), The mixing of Meddy "Sharon", in *Small-Scale Mixing in the Ocean*, edited by J. C. J. Nihoul and B. M. Jamart, *Elsevier Oceanogr. Ser.*, 46, 249–262.

Salat, J., and J. Font (1987), Water mass structure near and offshore the Catalan coast during the winter of 1982 and 1983, *Ann. Geophys., Ser. B*, *5*, 49–54.

Schroeder, K., G. P. Gasparini, M. Tangherlini, and M. Astraldi (2006), Deep and intermediate water in the western Mediterranean under the influence of the Eastern Mediterranean Transient, *Geophys. Res. Lett.*, *33*, L21607, doi:10.1029/2006GL027121.

Schroeder, K., A. Ribotti, M. Borghini, R. Sorgente, A. Perilli, and G. P. Gasparini (2008), An extensive western Mediterranean deep water renewal between 2004 and 2006, *Geophys. Res. Lett.*, *35*, L18605, doi:10.1029/2008GL035146.

Send, U., and J. Marshall (1995), Integral effects of deep convection, *J. Phys. Oceanogr.*, *25*, 855–872, doi:10.1175/1520-0485(1995)025 < 0855:IEODC>2.0.CO;2.

Speer, K., and E. Tziperman (1992), Rates of water mass formation in the North Atlantic Ocean, *J. Phys. Oceanogr.*, *22*(1), 93–104, doi: 10.1175/1520-0485(1992)022 < 0093:ROWMFI>2.0.CO;2.

Testor, P., and J. C. Gascard (2003), Large-scale spreading of deep waters in the Western Mediterranean sea by submesoscale coherent eddies, *J. Phys. Oceanogr.*, *33*(1), 75–87, doi:10.1175/1520-0485(2003)033 < 0075:LSSODW>2.0.CO;2.

Testor, P., and J. C. Gascard (2006), Post-convection spreading phase in the Northwestern Mediterranean Sea, *Deep Sea Res., Part I*, *53*, 869–893, doi:10.1016/j.dsr.2006.02.004.

Testor, P., et al. (2017), Multi-scale observations of deep convection in the northwestern Mediterranean Sea during winter 2012-2013 using multiple platforms, *J. Geophys. Res. Oceans*, doi:10.1002/2016JC012671.

Ulses, C., C. Estournel, P. Puig, X. Durrieu de Madron, and P. Marsaleix (2008), Dense shelf water cascading in the northwestern Mediterranean during the cold winter 2005: Quantification of the export through the Gulf of Lion and the Catalan margin, *Geophys. Res. Lett.*, *35*, L07610, doi:10.1029/2008GL033257.

Vargas-Yanez, M., P. Zunino, K. Schreder, J. L. Lopez-Jurado, F. Plaza, M. Serra, C. Castro, M. C. Garca-Martnez, F. Moya, and J. Salat (2012), Extreme Western Intermediate Water formation in winter 2010, *J. Mar. Syst.*, *105–108*, 52–59, doi:10.1016/j.jmarsys.2012.05.010.

Walin, G. (1982), On the relation between sea-surface heat flow and thermal circulation in the ocean, *Tellus*, *34*, 187–195, doi:10.1111/j.2153-3490.1982.tb01806.x.